Chemical Abundances of the Milky Way Thick Disk and Stellar Halo I.: Implications of [α/Fe] for Star Formation Histories in Their Progenitors

Miho N. Ishigaki

National Astronomical Observatory of Japan

2-21-1 Osawa, Mitaka, Tokyo 181-8588, Japan

ishigaki.miho@nao.ac.jp

Masashi Chiba

Astronomical Institute, Tohoku University

Aoba-ku, Sendai 980-8578, Japan

chiba@astr.tohoku.ac.jp

and

Wako Aoki

National Astronomical Observatory of Japan

2-21-1 Osawa, Mitaka, Tokyo 181-8588, Japan

aoki.wako@nao.ac.jp

ABSTRACT

We present the abundance analysis of 97 nearby metal-poor ($-3.3 <$[Fe/H]< -0.5) stars having kinematics characteristics of the Milky Way (MW) thick disk, inner, and outer stellar halos. The high-resolution, high-signal-to-noise optical spectra for the sample stars have been obtained with the High Dispersion Spectrograph mounted on the Subaru Telescope. Abundances of Fe, Mg, Si, Ca and Ti have been derived using a one-dimensional LTE abundance analysis code with Kurucz NEWODF model atmospheres. By assigning membership of the sample stars to the thick disk, inner or outer halo components based on their orbital parameters, we examine abundance ratios as a function of [Fe/H] and kinematics for the three subsamples in wide metallicity and orbital parameter ranges.

We show that, in the metallicity range of $-1.5 <$[Fe/H]≤ -0.5, the thick disk stars show constantly high mean [Mg/Fe] and [Si/Fe] ratios with small scatter. In contrast, the inner, and the outer halo stars show lower mean values of these abundance ratios with larger scatter. The [Mg/Fe], [Si/Fe] and [Ca/Fe] for the inner and the outer halo

stars also show weak decreasing trends with [Fe/H] in the range [Fe/H]> -2. These results favor the scenarios that the MW thick disk formed through rapid chemical enrichment primarily through Type II supernovae of massive stars, while the stellar halo has formed at least in part via accretion of progenitor stellar systems having been chemically enriched with different timescales.

Subject headings: Galaxy: formation — Galaxy: halo — Stars: abundances

1. Introduction

The Milky Way (MW) is widely recognized as a unique laboratory to test physical mechanisms of galaxy formation in the Universe as well as an underlying cosmology through observation of resolved stellar populations. In the context of galaxy formation theories based on the currently standard ΛCDM model, the MW is formed through accretions of smaller stellar systems like dwarf spheroidal (dSph) galaxies (e.g., Diemand et al. 2007). Numerical simulations have been performed to examine observable consequences of this process, implementing prescriptions of both assembly of dark matter halos and star formation within these halos. (Bullock & Johnston 2005; Robertson et al. 2005; Font et al. 2006a,b; De Lucia & Helmi 2008; Cooper et al. 2010). These studies generally suggest that the accreted galaxies imprint distinct substructures in both phase- and chemical abundance-space for many Gyrs (Font et al. 2006c; Johnston et al. 2008), demonstrating that the kinematics and chemical abundances are an important tracer of the merging history of the Galaxy.

Kinematics and chemical composition of nearby stars have provided one of the major constraints on the formation of the Galaxy ever since the landmark study of Eggen, Lynden-Bell & Sandage (1962). Currently available observational data on the phase-space structure of the Galactic stars show signatures of such accretion events of dSphs, as evidenced by spatial distribution and stellar populations of halo globular clusters (Searle & Zinn 1978; Mackey & Gilmore 2004; Lee et al. 2007), streams/overdensities in spatial distribution of stars (Ibata et al. 1994; Newberg et al. 2002; Majewski et al. 2003; Jurić et al. 2008), kinematic substructures (Helmi et al. 1999; Chiba & Beers 2000; Kepley et al. 2007; Dettbarn et al. 2007; Morrison et al. 2009; Klement et al. 2009; Starkenburg et al. 2009; Schlaufman et al. 2009; Xue et al. 2011), and a metallicity distribution of globular clusters (Cote et al. 2000). Photometric and spectroscopic studies based on the Sloan Digital Sky Survey (SDSS) further advanced our view of the Galaxy. The three-dimensional map out to the Galactocentric distance of $\sim$ 100 kpc provided by the SDSS shows that the substructures and stellar streams are ubiquitous, suggesting that the Galactic halo has formed, at least in part, through satellite accretions (Belokurov et al. 2006; Jurić et al. 2008; Bell et al. 2008; Klement et al. 2009). Carollo et al. (2010, 2007) reported that the stellar halo is divisible into two components, by studying spatial distributions, kinematics and metallicity of stars out to a several kpc from the Sun based on the SDSS data. Although the net-rotational velocity may be subject to some uncertainty in

the currently available data (see discussions in Schönrich et al. (2011); Beers et al. (2012)), at least growing number of observations suggest that the outer region of the Galactic halo contains a certain fraction of stars with extreme motions, that are difficult to account for with a single component halo (e.g., Kinman et al. 2012). These recent results highlight complex nature of the process taken place to form the Galactic halo.

To construct a concrete scenario for the MW formation, an important next step is examining whether the old Galactic components, namely, the thick disk and the stellar halo, are chemically divisible into subcomponents and, if so, getting insights about masses, luminosities, gaseous contents or time of accretions of progenitors of each subcomponent. Furthermore, it was proposed that not only stars accreted from dwarf galaxies, but also those formed "in situ" have played an important role in forming the current structure of the Galactic halo (e.g., Zolotov et al. 2010; Font et al. 2011). In order to make constraints on a relative contribution of these processes, detailed elemental abundances of stars belonging to each component provide useful signatures in addition to their phase-space structures and overall metallicities.

Detailed chemical abundance patterns of individual stars have been used as a fossil record of the star forming gas cloud at the stellar birthplace, which are likely conserved longer than the phase-space structure (e.g., Freeman & Bland-Hawthorn 2002). In particular, α-element-to-iron abundance ratios ([α/Fe]), where α usually stands for elements including O, Mg, Si, Ca and Ti, are commonly used to characterize nucleosynthesis and chemical enrichment history of a stellar population (Tinsley 1979; Matteucchi & Greggio 1986). This is based on the theory that α-elements are mainly synthesized in massive stars and ejected in Type II supernovae (SNe) within a short timescale, while Fe is ejected both in Type II and Type Ia SNe, for an extended period of time (time scale of Type Ia SNe is estimated to distribute from 0.1 Gyr to more than 10 Gyr; Kobayashi & Nakazato (2011)). Chemical enrichment of successive SNe II/Ia events finally form a characteristic trend in [α/Fe] with [Fe/H]. The trend can depend on various environment of star formation such as an efficiency that gas is converted to stars, ability that the system can retain their enriched metals or initial mass function (IMF; e.g., Lanfranchi & Matteucchi 2003). The [α/Fe]-[Fe/H] trend is, therefore, considered as a useful diagnostic to constrain chemical evolution of the structural components of the MW, including the thin disk (Edvardsson et al. 1993), bulge (Fulbright, McWilliam & Rich 2007; Bensby et al. 2009, 2011), thick disk (Bensby et al. 2003; Reddy et al. 2006; Bensby et al. 2007; Reddy et al. 2008), and stellar halo (e.g., McWilliam 1998; Cayrel et al. 2004; Lai et al. 2008; Hollek et al. 2011). Similarities and differences between these components were also investigated (Melendez et al. 2008; Bensby et al. 2010; Reddy et al. 2006). Studies on [α/Fe]-[Fe/H] trends further extended to the MW dwarf galaxies like relatively bright classical dwarfs (Shetrone et al. 2001; Tolstoy et al. 2003; Shetrone et al. 2003; Venn et al. 2004; Tolstoy et al. 2009; Aoki et al. 2009a; Kirby et al. 2011; Lai et al. 2011) and the recently discovered ultra-faint dwarfs (Koch et al. 2008; Feltzing et al. 2009; Norris et al. 2010). In particular, based on a homogeneous analysis of α-element abundances based on medium resolution spectra, Kirby et al. (2011) examined the trend in [α/Fe] with [Fe/H] of the individual dwarf MW

satellites to characterize their star formation history and its relation to the global properties like stellar/dynamical mass, luminosity of these galaxies. Such trend, therefore, is an important tracer of chemical enrichment in possible progenitors of the old components of our Galaxy, namely, the thick disk and stellar halo.

Previous studies on chemical abundances of nearby stars taking into account information on kinematics provide important insights into the hierarchical formation of the MW halo (Nissen & Schuster 1997; Stephens & Boesgaard 2002; Fulbright 2002; Gratton et al. 2003; Roederer 2008; Zhang et al. 2009; Ishigaki et al. 2010; Nissen & Schuster 2010, 2011). In particular, Nissen & Schuster (2010) (hereafter NS10) found the two distinct populations in the halo in terms of [α/Fe], namely "low-α" and 'high-α' stars, by performing a precise differential abundance analysis for the sample stars having similar metallicities and atmospheric parameters.

NS10 also found that the "low-α" stars tend to have higher orbital energies. This correspondence between abundances and kinematics implies that the low-α stars may represent accreted populations. In order to get more insights into the relation of these chemical inhomogeneity with formation history of each structural component of the MW, a homogeneous sample that includes stars having characteristic kinematics of the thick disk, inner, and outer halo components is necessary. Furthermore, the [α/Fe] ratios for these three components in a wide metallicity range allow us to examine possible trend of the [α/Fe] with [Fe/H], which has a significant implication to the star formation history in progenitors of each Galactic component.

In Zhang et al. (2009) and Ishigaki et al. (2010), we have presented an abundance analysis of stars whose orbits reach a distance larger than 5 kpc above and below the Galactic plane ($Z_{\rm max} > 5$ kpc) and compared their abundances with those of stars having smaller $Z_{\rm max}$ from literature. The comparison in the abundances was not straightforward because of the possible presence of the offset in the results between different studies. In this paper, we instead adopt the same methods as much as possible for all the sample here to avoid any related systematics. The sample used in this study is selected based on their kinematics so that the sample stars span a large range in kinematic parameters. In particular, the present sample includes stars having characteristic kinematics of the thick disk, inner, and outer halo stars classified based on the recent estimates of mean of three velocity components and their dispersions from Carollo et al. (2010).

Section 2 describes the selection of our sample and their kinematic properties. Then, Section 3 describes observation and reduction for the new sample. Section 4, provides detailed procedure of the estimation of stellar atmospheric parameters and elemental abundances. Section 5 and 6 show our main results on [α/Fe] and discuss implications on progenitors of the MW thick disk and the stellar halo.

2. The sample

2.1. Selection of the sample

The sample stars for our high-resolution spectroscopy were selected from the catalogs of Carney et al. (1994), Ryan & Norris (1991) and Beers et al. (2000). These catalogs include data on photometry, radial velocity, proper motions and metallicity estimates. Space motions, Galactic orbital parameters and distances for the stars in the catalogs were re-derived as described in Section 2.2.1.

In the present study, the stars having [Fe/H]< -0.5 and $V < 14.0$ mag were selected. In our previous studies (Zhang et al. 2009; Ishigaki et al. 2010), we have adopted the kinematic criteria of $Z_{\rm max}$, greater than 5 kpc, in order to select mainly the stars belonging to the outer stellar halo. We have supplement this sample with the stars having the orbital parameters characteristics of the thick disk and the inner stellar halo for the observing runs in 2010. The combined sample, which consists of stars having a wide range of metallicity and orbital parameters, is analyzed in a homogeneous manner. Therefore, this sample is suitable to examine the characteristic abundance patterns of the thick disk, inner, and outer stellar halos as a function of metallicity and orbital parameters with minimal systematic errors. Observations of the additional targets in 2010 are described in Section 3.

2.2. Kinematics of the sample

2.2.1. Orbital parameters

Velocity components in cylindrical coordinates (V_R, V_ϕ and V_Z), apo/peri-Galactic distances ($R_{\rm apo}$ and $R_{\rm peri}$) and maximum distances above/below the Galactic plane ($Z_{\rm max}$) were calculated as in Chiba & Beers (2000). In this calculation, proper motions were updated based on the revised *Hipparcos* for 76 stars (van Leeuwen et al. 2007), *Tycho-2* for 14 stars (Høg et al. 2000), UCAC2 for 5 stars (Zacharias et al. 2003), USNO-B for 2 stars (Monet et al. 2003), and LSPM-North catalog for 2 stars (Lépine et al. 2005). For the stars listed in both revised *Hipparcos* and *Tycho-2*, average proper motions and their errors are estimated following the method in Martin & Morrison (1998). Distances have been derived from *Hipparcos* parallaxes if their relative errors are less than 15 % (for 20 stars) and photometric ones for the remaining stars as in Beers et al. (2000). Radial velocities were updated to the values derived from the high-resolution spectra obtained in this study.

2.2.2. Membership probability

Using the orbital parameters obtained above, probabilities that each of the sample stars belongs to the thick disk, inner halo or outer halo component ($P_{\rm TD}$, $P_{\rm IH}$ and $P_{\rm OH}$, respectively) were

calculated from the following definition:

$$P_{\rm TD} = f_1(Z_{\rm max})\frac{P_1}{P}, \qquad P_{\rm IH} = f_2(Z_{\rm max})\frac{P_2}{P}, \qquad P_{\rm OH} = f_3(Z_{\rm max})\frac{P_3}{P} \tag{1}$$

where P and $P_i (i = 1, 2, 3)$ are given as

$$P = \Sigma f_i P_i, \tag{2}$$

$$P_i = K_i \exp\left[-\frac{(V_R - < V_{R,i} >)}{2\sigma^2_{R,i}} - \frac{(V_\phi - < V_{\phi,i} >)}{2\sigma^2_{\phi,i}} - \frac{(V_Z - < V_{Z,i} >)}{2\sigma^2_{Z,i}}\right] \tag{3}$$

$$K_i = \frac{1}{((2\pi)^{3/2}\sigma_{R,i}\sigma_{\phi,i}\sigma_{Z,i})}. \tag{4}$$

In the above definition of the membership probabilities, velocity distributions of the thick disk, inner, and outer halos (subscripts $i = 1, 2$, and 3, respectively) are assumed to be Gaussian with mean velocities ($< V_R >$, $< V_\phi >$, and $< V_Z >$) and dispersions (σ_R, σ_ϕ, and σ_Z) taken from the recent estimates based on the SDSS DR7 by Carollo et al. (2010). We also employ fractional contribution of each component, $f_i(Z_{\rm max}), i = 1, 2, 3$ in equation (1), which varies according to a given $Z_{\rm max}$ range (Carollo et al. 2010). The adopted values for these parameters from Carollo et al. (2010) are summarized in Table 1. Note that these parameters may be updated by the reanalysis of Beers et al. (2012), although the basic characteristics for each component have remained similar and it does not significantly affect the membership assignment in the present work. Additionally, we impose that $P_{\rm OH} = 1.0$ and $P_{\rm TD} = P_{\rm IH} = 0.0$ for the stars having $R_{\rm apo} > 15$ kpc, so that the star having an orbit with a low $Z_{\rm max}$ but a large $R_{\rm apo}$ is classified as an outer halo candidate. In equations (1), $P_{\rm TD}$, $P_{\rm IH}$ and $P_{\rm OH}$ are normalized so that they sum up to unity.

Of the observed sample stars, objects showing broad spectral lines, probably due to rapid rotation, or those turn out to be metal-rich stars ([Fe/H]> -0.5) as a result of our abundance analysis are excluded from the following analysis. As a result, 97 stars remain. Top panels of Figure 1 show the orbital parameters of the 97 sample stars in the $\log Z_{\rm max}$-V_ϕ (left) and V_ϕ-$(V_R^2 + V_Z^2)^{1/2}$ (right) planes. Crosses, filled circles and filled triangles indicate the sample stars with $P_{\rm TD} > 0.9$, $P_{\rm IH} > 0.9$, and $P_{\rm OH} > 0.9$, respectively. From now on, we will refer to the three subsamples as the "thick disk stars" for $P_{\rm TD} > 0.9$, "inner halo stars" for $P_{\rm IH} > 0.9$ and "outer halo stars" for $P_{\rm OH} > 0.9$. Open circles indicate objects whose kinematics are intermediate between the thick disk and the inner halo stars, namely, $P_{\rm TD}$, $P_{\rm IH} < 0.9$ and $P_{\rm TD}$, $P_{\rm IH} > P_{\rm OH}$. Similarly, open triangles indicate objects whose kinematics are intermediate between the inner and the outer halo stars, namely,$P_{\rm IH}$, $P_{\rm OH} < 0.9$ and $P_{\rm IH}$, $P_{\rm OH} > P_{\rm TD}$.

The thick disk stars in the sample have characteristic rotational velocities of $V_\phi \sim 180$ km s^{-1} and confined to $Z_{\rm max} < 1$ kpc. Some of stars with a small $(V_R^2 + V_Z^2)^{1/2}$ may have contaminated

from the thin disk component. The inner halo stars span a wide range in the rotational velocities with an average at $V_\phi \sim 0.0$ km s^{-1} and are dominant in $Z_{\rm max} < 10$ kpc. The outer halo stars show a larger dispersion in V_ϕ, some of which show extreme prograde or retro-grade rotation. These stars dominate in $Z_{\rm max} > 10$ kpc and in $R_{\rm apo} > 10$ kpc, which is characterized by high V_ϕ-$(V_R^2 + V_Z^2)^{1/2}$ velocities in the Solar neighborhood.

Bottom panels of Figure 1 show the distributions of $P_{\rm TD}$ (green), $P_{\rm IH}$ (blue) and $P_{\rm OH}$ (magenta) in $\log Z_{\rm max}$-V_ϕ and V_ϕ-$(V_R^2 + V_Z^2)^{1/2}$ planes. As expected from its definition, distribution of $P_{\rm TD}$ is peaked at $V_\phi \sim 180$ km s^{-1} and occupies the region of $Z_{\rm max} \leq 1$ kpc. $P_{\rm IH}$ spans $-150 < V_\phi < 150$ km s^{-1} and $Z_{\rm max} < 10$ kpc. $P_{\rm OH}$ spans a wider range in V_ϕ than $P_{\rm IH}$ and is dominant at $Z_{\rm max} > 10$ kpc.

Kinematic parameters for the sample stars and calculated $P_{\rm TD}$, $P_{\rm IH}$ and $P_{\rm OH}$ values are summarized in Table 2.

3. Observations and data reduction

3.1. Subaru/HDS observations

The high-resolution spectra were obtained in several observing runs during 2003 - 2010 with the High Dispersion Spectrograph (HDS; Noguchi et al. 2002) mounted on the Subaru Telescope. The spectra cover a wavelength range of about 4000-6800 Å except for ~ 100 Å at the gap between the two CCDs at ~ 5400 Å. For most of the sample stars, a spectral resolution is $R \sim 50000$, while spectra of some sample stars were taken with a higher resolution ($R \sim 90000$).

The data taken before 2010 have already been published (Zhang et al. 2009; Ishigaki et al. 2010). Summary of the new observation in 2010 (May 26 and June 18) is given in Table 3.

3.2. Data reduction

Bias correction, cosmic-ray removal, flat fielding, scattered light subtraction, wavelength calibration and continuum normalization were performed with standard IRAF routines by the same manner described in Ishigaki et al. (2010). The signal-to-noise ratios of the spectra per resolution element, after summing up for the spatial pixels, ranges from about 140 to about 390 at ~ 5000 Å (last column of Table 3). Equivalent widths (EW) of Fe I, Fe II, Mg I, Si I, Ca I, Ti I and Ti II lines are measured by fitting Gaussian to each absorption feature. The measured EWs for one of the sample stars, G 188-22, are in excellent agreement with those measured in NS10, with a root-mean-square deviation of 0.97 mÅ (Figure 2). The difference in EWs by < 1 mÅ typically affects the derived stellar abundances by < 0.03 dex, which is comparable to or smaller than the random errors estimated below. The measured EWs are summarized in Table 4.

4. Abundance analysis

The abundance analysis is performed using an LTE abundance analysis code as in Aoki et al. (2009b). In this work, effective temperatures ($T_{\rm eff}$) are estimated with the Infrared Flux Method (IRFM) as described in Section 4.3 instead of using excitation energies of Fe I lines as adopted in Ishigaki et al. (2010). This choice has been made to avoid getting unusually low $T_{\rm eff}$ and surface gravity ($\log g$) when these are constrained simultaneously using the Fe excitation energies and ionization balance, likely caused by non-local thermodynamic equilibrium (NLTE) effects on Fe abundances (Bergemann et al. 2011; Mashonkina et al. 2011). As an example, the iterative method adopted in Ishigaki et al. (2010) to constrain these parameters for CD-24 17504, one of the most metal-poor stars in our sample, converges at $T_{\rm eff} = 5821$ K and $\log g = 3.5$ dex, that are lowered by > 300 K and > 0.8 dex than those reported in literature (Aoki et al. 2009b; Nissen et al. 2007). Similar problem was noticed by Hosford et al. (2009) and suggested to be caused by departure from the assumption of LTE for metal-poor stars. Therefore, in the present study, we independently estimate $T_{\rm eff}$ using $V - K$ colors, while $\log g$ is estimated with the Fe I/Fe II ionization balance. Iterations are preformed over $\log g$, microturbulent velocity (ξ) and [Fe/H] so that these parameters are reproduced, while $T_{\rm eff}$ are fixed to their photometric estimates.

4.1. Atomic data

We have selected Fe I and Fe II lines from Ivans et al. (2006) and NS10 while their $\log gf$ values are taken mainly from Fuhr & Wiese (2006). We restrict the Fe I lines used for the abundance analysis to those having a laboratory measurement of the $\log gf$ value in the original references given in Fuhr & Wiese (2006). For Fe II lines, the $\log gf$ values are taken from Melendez & Barbuy (2009). Similarly, the lines of Mg, Si, Ca and Ti are selected from both Ivans et al. (2006) and NS10, while their $\log gf$ values are partly replaced based on Aldenius et al. (2007) and NIST for Mg I lines, Garz (1973) for Si I lines, Aldenius et al. (2009) for Ca I lines and Pickering et al. (2001) for Ti II lines. The number of lines used is larger than those used in Ishigaki et al. (2010) for most of the sample stars, although the line-to-line scatter is not significantly improved by the $\log gf$ updates. The adopted $\log gf$ values and their references are given in electronic form of Table 4.

4.2. Model atmospheres

Model atmospheres of Castelli & Kurucz (2003) are used in the abundance analysis. The model grid covers a range in the atmospheric parameter of our sample stars ($4000 < T_{\rm eff} < 6900$, $0.0 < \log g < 5.0$ and $-3.3 <$[Fe/H]< -0.5). For all of our sample stars we have used models with enhanced α element abundance of [α/Fe]=0.4. Although there are some sample stars with lower [α/Fe], the difference in the derived abundances from those obtained using a lower [α/Fe] model atmosphere is negligible, in the precision of the present analysis. The model atmospheres assume

a plane-parallel geometry (Castelli & Kurucz 2003), which may not be a good approximation for giants with low surface gravity (Heiter & Eriksson 2006). In order to test whether the low-gravity giants in our sample are affected by the geometry effect, we perform the abundance analysis for some of these stars using the MARCS model atmospheres (Gustafsson et al. 2008), which incorporate spherical geometry for low-gravity stars. The results of this analysis are described in Section 4.6.3 .

4.3. Effective temperature

The $T_{\rm eff}$ is estimated from *V-K* colors using metallicity-dependent calibrations of Casagrande et al. (2010) for the sample stars with $\log g > 3.5$ (dwarf and subgiants) and Ramírez & Meléndez (2005) for those with $\log g \leq 3.5$ (giants). *V* magnitudes and *E(B-V)* are taken from Carney et al. (1994), Ryan & Norris (1991) or Beers et al. (2000), while *E(B-V)* are revised to correct for the finite distance to the stars in the method of Beers et al. (2000). *K* magnitudes are taken from the Two Micron All Sky Survey (Cutri et al. 2003). For comparison, we have estimated the $T_{\rm eff}$ using Fe I lines by minimizing trend in derived abundances from individual Fe I lines with their excitation potentials (EPs) as has been done in Ishigaki et al. (2010). The result for the comparison is shown in Figure 3. The $T_{\rm eff}$ estimated from the *V-K* colors are higher than those from the excitation equilibrium by $\Delta T_{\rm eff} = 287$ K on average with a scatter $\sigma = 247$ K. This difference between photometric and spectroscopic $T_{\rm eff}$ is larger than those reported by Casagrande et al. (2010) for a sample of very metal-poor stars, $\Delta T_{\rm eff} = 177 \pm 33$ K or 240 ± 32 K with scatters $\sigma = 122$ K or 116 K, depending on the assumed surface gravity. As suggested by Casagrande et al. (2010) the $T_{\rm eff}$ from the excitation equilibrium strongly depend on an assumed value of the surface gravity. Therefore, the larger scatter in this work is likely caused by strong coupling between the excitation equilibrium $T_{\rm eff}$ and the surface gravity estimated from Fe I/Fe II ionization balance.

When the $T_{\rm eff}$ from the $V - K$ colors are adopted, non-negligible abundance-EP trends, that tend to be negative, appear as has been found by Lai et al. (2008) for their very metal-poor sample. Magnitude of the trends for the present sample is typically less than 0.1 dex eV^{-1} with a median value of -0.06 dex eV^{-1}. Mashonkina et al. (2011) examined the abundance-EP trends in a LTE and NLTE Fe I line abundance calculations for their sample of metal-poor stars and reported that the negative trends found by LTE analysis are reduced by the NLTE calculation. Therefore, in the assumption of LTE, the negative trends may not necessarily be resulted from an incorrect $T_{\rm eff}$ scale but may be caused by the NLTE effects.

The adopted $T_{\rm eff}$ values are given in Table 5.

4.4. Surface gravity and microturbulent velocity

The $\log g$ values are estimated based on Fe I / Fe II ionization balance as done by Ishigaki et al. (2010). We have checked the estimated $\log g$ for one of the sample star (G 188-22), which has relatively good *Hipparcos* parallax of $\pi = 9.03 \pm 1.68$ (van Leeuwen et al. 2007) in the method described in (Nissen, Hoeg & Schuster 1997). Assuming the $T_{\rm eff}$ and V_0 magnitudes estimated above and a stellar mass of $0.75 M_{\odot}$ for this star, the $\log g$ based on the *Hipparcos* parallax is $4.38^{+0.15}_{-0.18}$ dex (errors only from the parallax), which is in a good agreement with 4.52 dex, derived from the ionization balance. For some of the sample stars, the $\log g$ would exceed 5.0 if we attempt to get the same [Fe I/H] and [Fe II/H]. Since $\log g$ values higher than 5.0 are not expected from isochrones (e.g., Demarque et al. 2004), we simply adopt $\log g = 5.0$ for such stars.

The ξ is estimated so that the trend in iron abundances estimated from individual Fe I lines with the EWs is minimized as done by Ishigaki et al. (2010).

The adopted $\log g$ and ξ values are given in Table 5.

4.5. Abundances

The abundances of Mg, Si, Ca and Ti are determined from the measured EWs together with the revised $\log gf$ values as described in Section 4.1. Strong lines with reduced EWs ($\log {\rm EW}/\lambda$) greater than -4.7 (EW$\gtrsim$ 100 mÅ) are excluded from the analysis, because of their larger errors in the EW measurements and the saturation effects.

The derived abundances are normalized with the solar values from Asplund et al. (2009) to obtain the [X/H]. The [X/Fe] ratios are then derived by normalizing the [X/H] with [Fe I/H] or [Fe II/H] for neutral or ionized species, respectively.

Table 6 gives comparisons of the derived abundance ratios in this work with those from NS10 for nine sample stars, that are analyzed in common. The [Mg/Fe], [Si/Fe] and [Ca/Fe] are slightly lower than those from NS10. However, the mean difference is $\lesssim 0.1$ dex, which is comparable to the errors in the present work. The mean differences and standard deviations are $(\Delta[{\rm Mg/Fe}]_{\rm TW-NS10}, \sigma_{\Delta{\rm Mg}}) = (-0.08, 0.05)$, $(\Delta[{\rm Si/Fe}]_{\rm TW-NS10}, \sigma_{\Delta{\rm Si}}) = (-0.06, 0.07)$, $(\Delta[{\rm Ca/Fe}]_{\rm TW-NS10}, \sigma_{\Delta{\rm Ca}}) = (-0.10, 0.08)$ and $(\Delta[{\rm Ti/Fe}]_{\rm TW-NS10}, \sigma_{\Delta{\rm Ti}}) = (0.09, 0.03)$, indicating that the agreements are fairly good.

4.6. Errors

4.6.1. Scatters in abundances from individual lines

Random errors of the [X/Fe] ratios are estimated by dividing the standard deviation of the abundances from individual lines by a square-root of the number of lines used to compute the [X/H] values and adding the errors in [Fe I/H] ([Fe II/H] in the case of the ionized species) and those in the Solar abundance (Asplund et al. 2009) in quadrature. If only one line is available, then the standard deviation in the Fe I abundances, which are typically 0.04 to 0.13 dex, is adopted as a measure of the random error for that species.

4.6.2. Errors due to the atmospheric parameters

Additional errors due to the uncertainties in the adopted atmospheric parameters are examined by changing the parameters by $\pm\sigma_{T_{\rm eff}}$, $\pm\sigma_{\log g}$ and $\pm\sigma_{\xi}$. The $\sigma_{T_{\rm eff}} = 100$ K is adopted for all the sample stars, although the actual errors in $T_{\rm eff}$ may vary from object to object. The $\sigma_{\log g}$ and σ_{ξ} are assumed to be 0.3 dex and 0.3 km s^{-1}, respectively for all sample stars. Table 7 shows the result of this exercise for two dwarfs (G24–3, G64–37) and two giants (HD 215601, BD–18°271), having various metallicities in our sample. Typically, the deviations due to the change in the atmospheric parameters are less than 0.1 dex for dwarf stars, regardless of their metallicity. In the case of the two giant stars, [Fe I/H] ratios are sensitive to the change in $T_{\rm eff}$, such that $-1.40^{+0.14}_{-0.14}$ dex for HD 215601 and $-2.58^{+0.16}_{-0.17}$ dex for BD–18°271.

We quote the final errors as the quadratic sum of these contributions (errors due to the line-to-line scatter, $\sigma_{T_{\rm eff}}$, $\sigma_{\log g}$ and σ_{ξ}). The derived abundances and errors are summarized in Table 5.

4.6.3. Systematic errors due to the model atmospheres

Figure 4 shows $T - P_g$ relations of ATLAS/NEWODF (solid line) and MARCS (dashed lines for Plane-Parallel and a dotted line for Spherical) model atmospheres for three stars in our sample, G 24–3, HD 215601 and G 64–37. The model grids (T, $\log P_g$) have been interpolated to match the adopted atmospheric parameters. The differences in the derived abundance ratios are given in the last column of Table 7.

For G 24–3, which is a dwarf star with a metallicity of -1.4, the models of the ATLAS and MARCS Plane-Parallel are in good agreement. Resulting differences in abundance ratios are ≤ 0.06 dex, which is comparable to the precision of our analysis. In contrast, a giant star HD 215601 having a similar metallicity as G 24–3, the spherical MARCS model is cooler than the plane-parallel ATLAS/NEWODF model, at the upper atmospheric layers. This difference due to

the assumed geometry results in the [Fe I/H] abundance lower by 0.16 dex when the MARCS spherical model is adopted. We note that the line calculation in the present work still assumes the plane-parallel geometry even in the case that the spherical MARCS model is adopted. Therefore, it is possible that the deviation listed here is still different from the value that would be obtained by a fully consistent spherical analysis (Heiter & Eriksson 2006). Among the species examined for HD 215601, deviation in the [Fe I/H] ratios is the largest, likely because the Fe I are minor species in the atmosphere of this star. In contrast, Fe II, which is more dominant species, is relatively insensitive to the geometry effect. In total, the direction and magnitudes of the geometry effect on the [Fe I/H] and [Fe II/H] is in good agreement with the trend obtained by Heiter & Eriksson (2006) for the solar-metallicity case. For other element ratios, the geometry effect tends to cancel out and remains to be less than 0.1 dex. For G 64–37, which is more metal poor than the other two stars, the difference in the atmospheric structure is only evident in the upper layer in Figure 4 and resulting differences in the abundance ratios are ≤ 0.01 dex, which are almost negligible.

For these three sample stars, the differences in the atmospheric structures between the ATLAS and the MARCS model, as can be seen in Figure 4, result in difference in the abundance ratios comparable or much smaller than systematic errors from other sources (e.g., $T_{\rm eff}$, $\log g$ or ξ). As expected, the plane-parallel geometry would not be a very good approximation for giant stars as seen in the deviation in [Fe I/H] by > 0.1 dex when the MARCS spherical model is adopted instead of the ATLAS plane-parallel model for HD 215601. Such geometry effect is expected to be relatively small for lines with EW$\lesssim 100$ mÅ as mainly used in the present work in the examination by Heiter & Eriksson (2006) for a wide range of $T_{\rm eff}$ and $\log g$ with solar-metallicity. The effect is much smaller in atmospheres with lower metallicity as examined above. Furthermore, the effect tends to cancel out in part when the ratio of the two abundances of either neutral or ionized species is taken. Therefore, although full ranges in atmospheric parameters are not examined here, we adopt the ATLAS/NEWODF model atmosphere, assuming that the geometry effect remains to be small in the [X/Fe] ratios for our sample stars in order to keep homogeneity in the analysis method. For more high-precision analysis, however, especially for late-type giant stars, fully consistent analysis of spherical geometry is clearly desirable.

4.7. [X/Fe]-$T_{\rm eff}$ correlation

Our sample stars have a wide range of $T_{\rm eff}$ from 4000 to 6900 K. To examine any systematic differences in derived abundances for cool and warm stars, Figure 5 shows the [X/Fe] ratios plotted against the $T_{\rm eff}$ in the metallicity of [Fe/H]≥ -2 (left) and [Fe/H]< -2 (right). Size of the symbols corresponds to metallicity (e.g., larger symbols for higher metallicity). One may concern that apparent [X/Fe]-$T_{\rm eff}$ correlation could arise from possible correlation of [X/Fe] with [Fe/H]. This effect might be small because each of the warmer ($T_{\rm eff} > 5000$ K) and cooler ($T_{\rm eff} < 5000$ K) $T_{\rm eff}$ ranges contains a certain fraction of more metal-rich and more metal-poor stars and is not biased toward/against the particular metallicity stars.

In [Fe/H]< -2.0, significant positive correlation with a slope ~ 0.1 dex per 500 K can be seen for both [Ti I/Fe] and [Ti II/Fe]. Calculation of linear correlation coefficients, r, and their significance level ($P(r)$) for the null hypothesis of zero correlation is $P(r) < 0.001\%$ for the both species. The values of the slope are similar to those reported by Lai et al. (2008) for their sample of very metal-poor stars. Such trends may be attributed to NLTE effects on the Ti abundance as reported by Bergemann (2011). Marginal negative correlation with $T_{\rm eff}$ can be seen for the [Mg/Fe] and [Si/Fe] ratios in [Fe/H]≥ -2.0, although the slope is ~ 0.1 dex per 1000 K, which is comparable to the estimated errors of these abundance ratios. Care must be taken, however, in examining these abundance ratios as a function of [Fe/H] or orbital parameters so that the sample is not biased toward/against cooler or warmer stars.

To see whether each of the thick disk, inner, and outer halo subsamples, defined in Section 2.2.2, is biased toward/against stars with particular atmospheric parameters, Figure 6 shows the $\log g$-$T_{\rm eff}$ (left) and $T_{\rm eff}$-[Fe/H] (right) diagrams for the sample stars. Symbols are the same as in the top panels of Figure 1. It can be seen that the thick disk stars (green crosses) are predominantly giant stars while the inner (blue circles) and outer halo (magenta triangles) stars include larger number of dwarf stars. In particular, in a metallicity range of [Fe/H]> -1.5, the thick disk stars in the sample tend to be cooler than the inner and the outer halo stars.

The difference in typical $T_{\rm eff}$ between the thick disk, inner, and outer halo subsample might affect comparison in abundances between these subsamples. The average $T_{\rm eff}$ in the metallicity range of [Fe/H]> -1.5 is 5108 K for the thick disk, 5608 K for the inner halo and the 5676 K for the outer halo. According to the observed [Mg/Fe]-$T_{\rm eff}$ slopes in Figure 5, the lower $T_{\rm eff}$ by 500 K corresponds to the [Mg/Fe] by 0.06 dex, although the slope could also arise from possible intrinsic abundance difference between the thick disk and inner/outer stellar halos.

5. Results

5.1. Distribution of the sample stars in [X/Fe]-[Fe/H] planes

Left panels of Figure 7 and 8 show the [Mg/Fe], [Si/Fe], [Ca/Fe], [Ti I/Fe], [Ti II/Fe] and [Ti/Fe]=([Ti I/Fe]+[Ti II/Fe])/2 abundance ratios plotted against the [Fe/H] for the thick disk stars ($P_{\rm TD} > 0.9$; crosses), the inner halo stars ($P_{\rm IH} > 0.9$; filled circles) and the outer halo stars ($P_{\rm OH} > 0.9$; filled triangles). Symbols are the same as in Figure 1. Means (μ) and standard deviations (σ) of the abundance ratios for each of the thick disk and inner/outer halo stars within a given metallicity interval are summarized in Table 8. One object showing unusually high [X/Fe] ($0.5 - 0.6$ dex) values is excluded from this calculation and following discussion. Since this object shows a very large slope (~ 0.1 dex eV^{-1}) in the Fe I abundances versus EPs (See Section 4.3), the high [X/Fe] values are probably resulted from the incorrect $T_{\rm eff}$ adopted in the abundance estimate.

5.1.1. [Fe/H]> −1.5

In the metallicity range [Fe/H]> −1.5, the thick disk stars in the present sample show enhanced [Mg/Fe] and [Si/Fe] ratios at the means larger than 0.3 dex with very small scatters ($\sigma \leq 0.07$ dex; Table 8). The constantly high values of these abundance ratios for the thick disk stars with [Fe/H]< −0.5 are consistent with those reported in previous studies (e.g., Bensby et al. 2003). In contrast, the inner and the outer halo stars in the present sample show the [Mg/Fe] and [Si/Fe] ratios $\lesssim 0.2$ dex, which is lower than the thick disk stars. The scatter for these stars is much larger ($\sim 0.12 - 0.13$ dex) than that of the thick disk stars, although contribution from the measurement errors is not ruled out. A Kolmogorov-Smirnov test yields that the probability for a null hypothesis that the [X/Fe] ratios of the thick disk stars are drawn from the same distribution as those of the inner halo stars is 2 % for [Mg/Fe] ratios and 3 % for [Si/Fe] ratios. Similarly, the null hypothesis for the thick disk and the outer halo is rejected at the level of < 1 % for both [Mg/Fe] and [Si/Fe] ratios.

To examine whether the observed difference in the [Mg/Fe] and [Si/Fe] ratios between the thick disk and inner/outer halo stars is caused by the difference in typical $T_{\rm eff}$ between these subsamples as described in Section 4.7, a comparison was performed using a limited sample of giant stars ($T_{\rm eff} \leq 5500$ and $\log g \leq 3.5$) in a metallicity range of [Fe/H]> −1.5, which includes six thick disk, four inner halo and two outer halo stars. As a result, the differences in the mean [Mg/Fe] and [Si/Fe] values between the thick disk and the outer halo remained to be ~ 0.1 dex, while the difference in the mean values between the thick disk and the inner halo vanishes. Although this comparison needed to be confirmed with a larger sample, this result may indicate the importance of understanding systematic errors in derived abundances between dwarfs and giants. In the highest metallicity of [Fe/H]> −1.0, differences in the [Mg/Fe] and [Si/Fe] for the four thick disk stars and the two inner halo stars are significantly large (~ 0.3 dex), which cannot be explained by the difference in the typical $T_{\rm eff}$ alone.

In the precise differential analysis of NS10, the sample stars in this metallicity range are separated into the 'high-α' and the "low-α" stars, defined based on the [Mg/Fe] ratios. The presence of the chemically distinct components in halo stars could not be evaluated in the present work because of the lower internal precision as described above. The inner halo stars kinematically resemble the high-α stars in NS10. Some of the inner halo stars in the present sample have high [Mg/Fe] similar to the thick disk stars, while the two most metal-rich inner halo stars show low [Mg/Fe], [Si/Fe] and [Ca/Fe]. The outer halo stars, that kinematically resemble the low-α stars in NS10, generally show lower [Mg/Fe] in their highest metallicity range and the overlap with the thick disk stars is small.

The [Ca/Fe] ratios for the thick disk, inner, and outer halo stars show largely overlapping distributions. In particular, for the thick disk stars, the mean [Ca/Fe] ratio is lower than the [Mg/Fe] and [Si/Fe] ratios by ~ 0.1 dex (Table 8). Such a low [Ca/Fe] relative to [Mg/Fe] seen in the thick disk stars, where the mean [Ca/Mg] ratio less than the solar value, is not seen in the

inner and outer halo stars, where the mean [Ca/Mg] is $\geq$0.00.

For all of the thick disk, inner, and outer halo subsamples, the [Ti II/Fe] ratios are $\gtrsim$ 0.1 dex larger than the [Ti I/Fe] ratios. Such an effect is also reported by previous studies (e.g., Lai et al. 2008). This may indicate that an ionization balance assumed in the LTE analysis is not valid for Ti (Bergemann 2011).

5.1.2. [Fe/H]< −1.5

In the metallicity range of [Fe/H]< -1.5, the thick disk stars are rare and the halo stars dominate. The thick disk stars in this metallicity range, again, show higher [Mg/Fe] ratios (> 0.3 dex) than the inner/outer halo stars with a small scatter. Both of the inner and the outer halo stars show a wider range in these element ratios from the near-solar value to [X/Fe]$\sim$ 0.5 than seen in the thick disk stars. The scatter in the abundance ratios is similar to that of the higher metallicity for all of the three subsamples, except for extremely metal-poor stars ([Fe/H]< -3.0).

The [Mg/Fe], [Ca/Fe], [Ti I/Fe] and [Ti II/Fe] values of the sample stars in this metallicity range generally agree with previous studies by Cayrel et al. (2004), Lai et al. (2008) and Bonifacio et al. (2009), which are shown in Figures 7 and 8 with dotted, dash-dotted and dashed lines, respectively. The [Si/Fe] ratios are slightly higher in this study. One of the reasons for this discrepancy could be the difference in the Si I lines used: these studies mainly use the Si I line at 3905.53 Å while the present study uses redder lines. In fact, if we use the same EWs and $\log gf$ values as those used in Lai et al. (2008) for their one sample star, BD+03 740, our abundance analysis adopting the same atmospheric parameter results in [Si/Fe]$= 0.12$, which is in good agreement with the value of [Si/Fe]$= 0.07$ from Lai et al. (2008) within the quoted error.

5.1.3. [X/Fe]-[Fe/H] trend

A trend in the [X/Fe] with [Fe/H] is frequently interpreted as a tracer of chemical evolution of a self-enriched stellar system (Tinsley 1979; Matteucchi & Greggio 1986; Gilmore & Wyse 1991). It is particularly interesting whether the abundance ratios for the thick disk, inner, and the outer halo stars show different trends, which could be evidence of different star formation history of their progenitors. In order to examine the trend for the present sample, the right panel of Figures 7 and 8 plot the weighted means of the abundance ratios within a given [Fe/H] interval for each of the subsamples. The error bars correspond to the error in the weighted means of these abundance ratios.

In [Fe/H]> -2.5, the [Mg/Fe], [Si/Fe] and [Ca/Fe] ratios for the inner and the outer halo stars slightly decrease with [Fe/H]. The thick disk stars also show hints of decreases at the highest metallicity bin. This apparent offset, however, could be caused by contamination of thin disk stars

that are known to have lower [α/Fe] (Lee et al. 2011). According to our criteria (Section 2.2.2), stars having disk-like kinematics are all classified as thick disk stars, although thin disk stars may present in the range [Fe/H]> -0.5.

The [Ti I/Fe] and [Ti II/Fe] ratios do not show such a decreasing trend but stay constant in [Fe/H]> -2.5 for all of the three subsamples. The absence of the [Ti/Fe]-[Fe/H] trend may result from production of Ti in Type Ia SNe together with Fe, in contrast to other α elements like O or Mg, that are predominantly enriched via Type II SNe.

In [Fe/H]< -2.5, the [X/Fe]-[Fe/H] trends are not seen for the three subsamples within the error bars. The absence of the trend is expected if the chemical enrichment predominantly occurred through Type II SNe (Kobayashi et al. 2006). We note that in this low metallicity, the outer halo stars having a large retro-grade orbit ($V_\phi < -100$ km s^{-1}) have similar abundance ratios as those of the typical inner halo stars with similar metallicity on average.

5.2. Correlation in the [X/Fe] ratios with kinematics

Figures 9 shows the [X/Fe] ratios of the thick disk, inner, and outer halo stars plotted against the orbital parameters, V_ϕ, $\log Z_{\rm max}$, $\log R_{\rm apo}$ and eccentricity (e). Symbols are the same as in Figure 7. Solid and dashed lines connect means and means $\pm$ standard deviations, respectively, within a given interval of each orbital parameter. Left and right panels in each diagram show the plots for $-1.5 <$[Fe/H]≤ -0.5 and $-2.5 <$[Fe/H]≤ -1.5, respectively. This separation is made so that any [X/Fe]-[Fe/H] correlation would not produce apparent [X/Fe] correlation with the orbital parameters. For example, because fraction of the outer halo stars increases at lower metallicity, the possible increase in the [Mg/Fe] with the decreasing [Fe/H] would result in high [Mg/Fe] for such outer halo stars having large $R_{\rm apo}$ or $Z_{\rm max}$.

In the [X/Fe]-V_ϕ plot (top left), finite correlation is seen in the increasing [Mg/Fe] with V_ϕ at $-1.5 \leq$[Fe/H]< -0.5. In this metallicity range, probability for null correlation is less than 0.1 % according to the calculated linear correlation coefficient. This can partly be explained by the difference in [Mg/Fe] between the thick disk and the halo stars; the former have high $V_\phi \sim 200$ km s^{-1} while the latter span a wide range in V_ϕ as mentioned in Section 5.1.1. If the thick disk stars are excluded from the calculation of the correlation coefficient, the probability for the null correlation is increased to 4 %.

In the [X/Fe]-log($Z_{\rm max}$) plot (top right), the correlation is not significant for these abundance ratios. The [Mg/Fe] ratios are slightly lower in $Z_{\rm max} > 1$ kpc in $-1.5 <$[Fe/H]≤ -0.5, probably because of the absence of the thick disk stars, that have high [Mg/Fe], at high $Z_{\rm max}$.

In the [X/Fe]-log($R_{\rm apo}$) plot (bottom left), the apparent correlation is seen only for the [Ti II/Fe] in $-2.5 <$[Fe/H]≤ -1.5. A negative correlation in the [Mg/Fe] versus log($R_{\rm apo}$) also cannot be ruled out; the probability for the null correlation is 11 %. Stephens & Boesgaard (2002)

suggested the decreasing trend of [α/Fe] (=[(Mg+Si+Ca+Ti)/Fe]) with $R_{\rm apo}$ based on their sample of halo stars covering a similar metallicity range as the present study, although the observed trend is rather small (0.1 dex per decade). Since their study as well as the present study use bright local sample, the number of the outer halo stars is still not large enough to conclude on this subject.

In the [X/Fe]-e plot (bottom right), a decreasing trend of the [Mg/Fe] with e at $-1.5 <$[Fe/H]≤ -0.5 can be seen. This trend is significant at the level that the probability for the null correlation is less than 0.1 %. The probability is remained to be significant after the thick disk stars are excluded (< 3 %). This result is in qualitative agreement with that of Schuster et al. (2011), who show that low-α stars dominate at the large maximum eccentricity, $e_{\rm max} \geq 0.85$.

5.3. The membership probabilities in the [X/Fe]-[Fe/H] diagram

In previous sections, we have simply defined the thick disk, inner, and outer halo stars as being $P_{\rm TD} > 0.9$, $P_{\rm IH} > 0.9$ and $P_{\rm OH} > 0.9$, respectively. Although these cuts are useful to select potential candidates of members of the each Galactic component, they remove the sample stars with intermediate kinematics from the interpretation of the [X/Fe]-[Fe/H] diagnostics. The difference and similarities in the [X/Fe] between the three subsamples have only been discussed based on the means and the standard deviations within a given metallicity range for these limited sample stars (Table 8). To maximize the use of the [X/Fe]-[Fe/H] diagrams, taking into account all of the sample stars with proper weights, we examine the distribution of the $P_{\rm TD}$, $P_{\rm IH}$, and $P_{\rm OH}$ on the [X/Fe]-[Fe/H] plane.

Figure 10 shows distribution of $P_{\rm TD}$ (green), $P_{\rm IH}$ (blue) and $P_{\rm OH}$ (magenta) in the [X/Fe]-[Fe/H] planes. Each contour shows sum of the membership probabilities within a given [X/Fe] and [Fe/H] bin. This figure illustrates difference and similarity in distribution for the thick disk, inner, and outer halo components, in the [X/Fe]-[Fe/H] planes. We note that there may be a selection bias in [Fe/H], since only stars with [Fe/H]< -0.5 are included in our sample. Therefore, the distribution of the [Fe/H] is not representative of a true underlying distribution of the thick disk, inner, and outer halo populations. We therefore, restrict our discussion on the difference in the [X/Fe] for the three subsamples in a given metallicity range.

As implied from the previous sections, the [Mg/Fe] and [Si/Fe] show similar trends with [Fe/H] for each of the $P_{\rm TD}$, $P_{\rm IH}$ and $P_{\rm OH}$. The membership probability for the thick disk ($P_{\rm TD}$) shows a narrow distribution in the [Mg/Fe] and [Si/Fe] peaked at $\sim$ 0.3 in a range $-1.5 <$[Fe/H]< -0.5. In contrast, the membership probability for the inner halo ($P_{\rm IH}$) shows significantly broader [Mg/Fe] and [Si/Fe] distributions, that are largely overlap with the distributions for the $P_{\rm TD}$. The membership probability for the outer halo ($P_{\rm OH}$) shows overlapping distribution with those of the $P_{\rm IH}$, but peaked at relatively low [Mg/Fe] and [Si/Fe] with smaller dispersion than the $P_{\rm IH}$. It can also be seen that the peak in the [Mg/Fe] and [Si/Fe] for the $P_{\rm OH}$ gradually shifts from $\sim$ 0.4 in [Fe/H]< -2 to $\sim$ 0.2 in [Fe/H]> -1.5. The distribution for the $P_{\rm IH}$ and $P_{\rm OH}$ is indistinguishable

in the lower metallicity range ([Fe/H]< -2.0)

In the [Ca/Fe]-[Fe/H] plot, the distributions for $P_{\rm TD}$,$P_{\rm IH}$ and $P_{\rm OH}$ largely overlap with each other and clear distinctions of the peak position in [Ca/Fe] between the three probabilities are not seen. This behavior is similar in the [Ti I/Fe] and [Ti II/Fe]-[Fe/H] diagram except that the $P_{\rm IH}$ and $P_{\rm OH}$ appear to show double peaks at [Fe/H]~ -1.3.

In total, if all of the three subsamples are considered, distribution in the [X/Fe]-[Fe/H] plane is roughly peaked at constant [Mg/Fe] in a wide metallicity range ($-3.5 <$[Fe/H]< 0.5). However, when the thick disk, inner, and outer halos are separately considered as in Figure 10, differences in distribution are seen for [Mg/Fe] and [Si/Fe] ratios.

6. Discussion

We summarize the main results of the present study as follows.

- The thick disk stars show relatively high [Mg/Fe] and [Si/Fe] ratios compared to the inner and outer halo stars for [Fe/H]> -1.5.
- The inner halo stars show a mean [Mg/Fe] and [Si/Fe] ratios lower than the thick disk stars with larger scatter.
- The outer halo stars show similarly low mean [Mg/Fe] and [Si/Fe] ratios as the inner halo stars, which is lower than those of the thick disk stars. The outer halo stars (and the part of the inner halo stars) also show a hint of a decreasing trend in [Mg/Fe], [Si/Fe] and [Ca/Fe] with [Fe/H] in [Fe/H]> -2.5.
- The three subsamples show largely overlapping distribution in [Ca/Fe], [Ti I/Fe] and [Ti II/Fe].
- Correlation of the [Mg/Fe] ratios with the orbital eccentricity e is seen in $-1.5 \leq$[Fe/H]< -0.5 at a significant level. For other orbital parameters (V_ϕ, $Z_{\rm max}$, $R_{\rm apo}$), significant correlation with [X/Fe] is not clearly seen.

In the following subsections, we first compare the results for the [Mg/Fe], [Si/Fe] and [Ca/Fe] ratios with those obtained for stars belonging to the MW dwarf satellite galaxies. Finally, we discuss the implications of the present result for the formation of the MW thick disk and stellar halo.

6.1. Comparison with the chemical abundances of the MW dwarf satellites

Tolstoy et al. (2009) review recent data on the abundances for the MW dwarf satellites including Fornax, Sculptor, Sagittarius and Carina dSphs. In [Fe/H]> -1.5, the thick disk, inner,

and outer halo stars in the present sample show higher [Mg/Fe] than those seen in the stars in the dSphs. For example, the Sculptor dSph shows a near solar average value of the [Mg/Fe] ratio at [Fe/H]~ -1.5 (Tolstoy et al. 2009), while the inner and the outer halo stars at this metallicity show the average [Mg/Fe] of $\sim 0.1 - 0.2$ (Table 8). The difference becomes more substantial at higher metallicity, where the [Mg/Fe] decreases with metallicity in Sculptor, reaching the sub-solar mean [Mg/Fe] ratio at [Fe/H]> -1.0. As can be seen in Figure 9, the sample stars having either extreme retrograde orbits, high $Z_{\rm max}$ or $R_{\rm apo}$, which are the most likely candidates of the accreted stars, do not show the [X/Fe] ratios significantly lower than the solar values. This difference in abundance ratios between the field halo and dSph stars implies that the halo progenitors had different chemical enrichment history from surviving dSphs in terms of star formation rate, galactic wind efficiency or duration and frequency of major star formation episodes that drive chemical enrichment of these systems. In the case of Sculptor, Kirby et al. (2011) show that the [α/Fe]- [Fe/H] relation for their medium resolution spectroscopic sample is well reproduced by a model with a low star formation rate, low initial gas mass and the $\sim$ 1 Gyr duration of star formation which may have started more than 10 Gyr ago. This scenario suggests that the chemical enrichment of the system proceeds slowly so that the overall metallicity of the system remained low when Type Ia SNe start to enrich the system with Fe (Tolstoy et al. 2009). The inner and outer halo stars show modest decreasing trends in these abundance ratios likely starting at [Fe/H]> -2.0. The trends, however, are much shallower than those seen in Sculptor. This result may suggest that the possible progenitors of the inner and outer halo stars have stopped forming stars before the enrichment from Type Ia SNe became significant.

In [Fe/H]< -2.0, the number of stars studied for individual abundances is smaller, probably because of the relative scarcity of very metal-poor stars in the well-known classical dSphs. Some of the extremely metal-poor stars in the Sextans dSphs show near-solar [Mg/Fe] ratios (Aoki et al. 2009a), that are lower than the inner and the outer halo stars in the present sample. On the other hand, recently discovered ultra-faint dSphs generally show super-solar values of the [Mg/Fe] similar to the inner/outer halo stars (Tolstoy et al. 2009). Given that these observed dSphs show a wide range of [Mg/Fe] ratios from near-solar to $\sim$ 1.0, the scatter in the [Mg/Fe] in both the inner and outer halo stars are relatively small (< 0.15 dex). A larger sample in this low metallicity range is desirable to characterize the abundance ratios and their scatter in the MW halo in comparison with the dSphs.

Different behavior of [Ca/Fe] and [Ti/Fe] ratios from those of [Mg/Fe] and [Si/Fe] were previously noted for the stars in the MW dwarf satellite galaxies (e.g., Venn et al. 2004). Letarte et al. (2010) show that the trend of the lower [Ca/Fe] and [Ti I/Fe] than [Mg/Fe] or [Si/Fe] for red giant stars is seen in Fornax dSph. They suggest that this discrepancy come from either different nucleosynthetic origins of Ca and Ti from those of Mg and Si or significant dependence of Type Ia SNe Ca and Ti yields on metallicity. The latter possibility is unlikely because if the Type Ia SNe have contributed significantly to the chemical evolution of the thick disk, the [Mg/Fe] ratios would decrease as the [Fe/H] increases, which is inconsistent with the observed high [Mg/Fe] ratios for the

thick disk stars in the present sample. If the former is mainly responsible for the low [Ca/Fe] and [Ti I/Fe] ratios, the thick disk stars would be formed in the progenitors that have been enriched more with Mg and Si from hydrostatic C and O burning than with Ca and Ti from explosive nucleosynthesis in SNe.

6.2. Implication for the formation of the MW old components

The constantly high [Mg/Fe] and [Si/Fe] ratios of the thick disk stars, unlike the observed dSphs, suggest that these are predominantly enriched with Type II SNe (Kobayashi et al. 2006). This suggests that the initial star formation in the progenitor of the thick disk stars was high enough to enrich the system to [Fe/H]> -1 and short enough to complete before Type Ia SNe produce significant Fe. The low [Ca/Mg] ratios observed for the thick disk stars are in qualitative agreement with those expected from the Type II SNe yields integrated over progenitor stellar masses with Salpeter IMF in Tsujimoto et al. (1995), supporting enrichment in the thick disk progenitors has occurred predominantly via Type II SNe. Thick disk stars in the solar neighborhood are also known to be old (age ≤ 12 Gyr) suggesting that the star formation took place at the early stage of the MW formation (Fuhrmann 2011).

Several mechanisms are proposed for the origin of the halo stars, in the context of the hierarchical galaxy formation scenario. First, the halo stars could be formed through dissipative collapse of gaseous material on to the central region of the Galaxy, often referred to as "in situ" stars (Zolotov et al. 2010; Font et al. 2011). This could be achieved either via rapid collapse of primordial gas on to the Galactic dark matter halo or through early major mergers of gas-rich galaxies. In such a system, high star formation rate is triggered by shocks in the interstellar medium (ISM) and, as a result, metal enrichment proceeds primarily through Type II SNe with a short time-scale comparable to the age of massive stars ($< 10^6 - 10^7$ yr). Thus, this process would yield stars with high [α/Fe]. In the present study, such high-[α/Fe] stars are found both in the thick disk and the inner halo subsamples, as seen in the [Mg/Fe] and [Si/Fe]-[Fe/H] plots in the left panel of Figure 7. This result suggests that a sizable fraction of the inner halo stars were formed out of gas enriched rapidly via Type II SNe before Type Ia SNe became a significant contributor to metals in the ISM, similar to the thick disk stars.

The second possibility is that the halo stars were originally formed within isolated dwarf galaxies that are later accreted to the Galaxy. The accreted dwarf galaxies would be tidally disrupted as they orbit around the Galaxy. The debris stars then populated the halo while kept their orbital velocity similar to their disrupted host galaxies. In this case, the stellar mass of the halo grows more slowly than the former case. Chemical abundance of the halo stars, then, would reflect metal-enrichment history in their progenitor dwarf galaxy, that would have less efficient star formation history because of their shallower potential well than that of the Galaxy, which makes the enriched gas easier to escape. Since many of the surviving MW dwarf satellites show lower [α/Fe] that are indicative of their lower star formation rate, it is naively expected that the halo stars would

also have lower [α/Fe] ratios if the major fraction of the halo stars have been accreted from such a system. In the present study, the lower [Mg/Fe], [Si/Fe] or [Ca/Fe] in [Fe/H]> -1.5 than the thick disk subsample is found for both the inner and the outer halo subsamples. The lower [α/Fe] for some of the inner and outer halo stars may indicate that the progenitors of these stars have enriched with metals via Type Ia SNe and/or galactic winds are efficient in ejecting metals out of the system, as suggested for the MW dwarf satellites (Kirby et al. 2011). Then, the decreasing [Mg/Fe] with increasing e seen in Figure 9 could be interpreted as fraction of the accreted stars might increase with e in the present sample.

Even though some halo star in our sample show relatively low [α/Fe], that is not as significant as found in stars in the dwarf galaxies as mentioned in Section 6.1. The difference in the [α/Fe] ratios between the MW stellar halo and the dwarf satellites can be explained if the progenitors of the stellar halo have been accreted early on stopping its star formation, while the surviving satellites have chemically enriched for a longer time (Font et al. 2006a). The implication from the simulation of Font et al. (2006c) further suggests that the lack of large-scale gradients in the [α/Fe] (Figure 9) supports the early accretions ($\gtrsim$ 10 Gyr ago) for the MW halo. The apparent lack of the [α/Fe] correlation with $\log Z_{\rm max}$ and $\log R_{\rm max}$ may support the early accretion scenario. The quiescent accretion history of the MW halo for the last $\sim$ 10 Gyrs is also supported by the recent finding of Schuster et al. (2011) that their sample of metal-rich halo stars at [Fe/H]~ -1, are older than $\sim$ 10 Gyrs, including relatively younger "low-α" stars.

Purcell et al. (2010) suggest another origin of the halo stars; disk stars can be dynamically heated to become halo stars via minor mergers on the disk plane. In the present sample, the stars classified as having the intermediate kinematics between the thick disk and the inner halo stars, shown in the open blue circles in Figure 7, show relatively high [Mg/Fe] ratios similar to the thick disk stars. This result suggests that the stars having moderately disk-like orbit could have been formed in a rapid star formation event like the thick disk stars.

Cosmological simulations of Zolotov et al. (2010) and Font et al. (2011) suggest that a hybrid scenario for the halo formation is naturally expected in the hierarchical formation of the MW. More specifically, recent hydrodynamical simulations of Font et al. (2011) suggest that, at a Galactocentric distance grater than 20 kpc, where the halo component dominates over the bulge component, about 20% of stars may have formed in situ, while the other fraction of stars formed within satellite galaxies.

The possible boundary at which transition in the dominant progenitors ("in situ", accreted dSph, heated disk) may occur is not very well constrained in the present study. If any, the question of whether the transition occurs sharply or mildly would be important in constraining the merging history of our Galaxy. More qualitative conclusion on this issue should only be made after the sample is significantly expanded. Current sample stars are all located in the solar neighborhood (< 2 kpc), in which the fraction of the halo stars is very low. Obviously, larger volumes in the halo should be investigated in order to construct a sample representative of the halo population. Since

high resolution spectroscopy is not efficient for a larger sample including distant objects beyond the solar neighborhood, lower resolution spectroscopy combined with a sufficient analysis scheme (e.g., Kirby et al. 2010; Lee et al. 2011; Ruchti et al. 2011) would be extremely useful to explore properties of the more distant halo. Recently discovered substructures in the stellar halo would be possible candidates of recent accretion events, whose [α/Fe] would give information on their progenitors.

α-element alone may not be enough to constrain the chemical evolution of stellar system, since enrichment mechanisms other than Type II/Ia SNe are also thought to have played an important role. For example, the importance of neutron-capture elements that are synthesized via slow-neutron capture in the asymptotic giant branch stars has been emphasized in chemical evolution models (e.g., Lanfranchi, Matteucchi & Cescutti 2008) and the observation of the dwarf satellites showing significant Ba enhancement. Analysis of such neutron-capture elements as well as iron peak elements will be presented in the forthcoming paper (M. N. Ishigaki et al. in preparation).

7. Conclusion

We have presented the abundances of Fe, Mg, Si, Ca and Ti for 97 metal-poor stars covering a wide range of metallicity ($-3.3 <$[Fe/H]< -0.5) and orbital parameters, including those having the extreme outer halo kinematics. The abundances were obtained from the high-resolution spectra taken with Subaru/HDS using a one-dimensional LTE abundance analysis code with Kurucz model atmospheres. Our results provide insights about differences and similarities in the [α/Fe] ratios as a function of [Fe/H] and the kinematics among the three presumably old Galactic components, the thick disk, inner, and outer stellar halo as summarized below:

- The thick disk stars show high [Mg/Fe] and [Si/Fe] ratios than the inner and outer halo stars in their overlapping metallicity range ([Fe/H]> -1.5). The high abundance ratios for Mg and Si, that are predominantly synthesized in massive stars, are in good agreement with previous studies. This result suggests that the thick disk stars were formed out of gas primarily enriched by Type II SNe of massive stars with little contribution of Fe from Type Ia SNe.

- The inner halo stars span a wide range in [Mg/Fe] and [Si/Fe] ratios compared to the thick disk stars. The results imply that the inner halo stars have formed in various formation sites, presumably including the collapsed gas in the early Galaxy or dwarf galaxies accreted early times.

- The outer halo stars show similar mean [Mg/Fe] and [Si/Fe] ratios as the inner halo stars, which is lower than those of the thick disk stars. The inner and the outer halo stars together show a hint of a decreasing trend in [Mg/Fe], [Si/Fe] and [Ca/Fe] with [Fe/H] in [Fe/H]> -2.0. These results suggest that the contribution from Type Ia SNe may have played some role in the chemical evolution of the outer halo progenitor.

- The three subsamples show largely overlapping distributions in the [Ca/Fe], [Ti I/Fe] and [Ti II/Fe] versus [Fe/H] diagrams. The different nucleosynthesis site for these two elements from that of Mg and Si may explain this result. However, because of the large errors in [Ti I/Fe] and [Ti II/Fe], presumably due to the NLTE effects, definitive conclusions from the Ti abundances cannot be made in the present study.

- Significant correlation of the [X/Fe] ratios with the orbital parameters (V_ϕ, $Z_{\rm max}$, $R_{\rm apo}$) is not observed in the present sample, except for the decreasing [Mg/Fe] trend with the increasing e in $-1.5 <$[Fe/H]≤ -0.5. This result suggests that dwarf galaxies having low [X/Fe] ratios have not significantly contributed to build up the present-day stellar halo. Since this conclusion is drawn only from the local sample, the abundance data for a larger volume of the Galaxy are desirable to evaluate the large-scale abundance gradient.

More quantitative conclusions on the large-scale distribution of [α/Fe] are expected by next-generation multi-object spectroscopic surveys that cover a larger volume of the MW thick disk and stellar halo.

The authors thank the referee for her/his constructive comments and useful suggestions that have helped us to improve our paper. We thank A. Tajitsu, T-S. Pyo and the staff members of Subaru telescope for their helpful support and assistance in our HDS observation. MI is grateful to U. Heiter, A. Korn and B. Edvardsson for the important suggestions on the abundance analysis and for the kind hospitality. M.I. is also grateful to P. E. Nissen for the valuable discussion and comments. This work is supported in part from Grant-in-Aid for Scientific Research (23740162, 23224004) of the Ministry of Education, Culture, Sports, Science and Technology in Japan.

Facilities: Subaru (HDS).

REFERENCES

Aldenius, M., Tanner, J. D., Johansson, S., Lundberg, H. & Ryan, S. G. 2007, A&A, 461, 767

Aldenius, M., Lundberg, H. & Blackwell-Whitehead, R. 2009, A&A, 502, 989

Aoki, W., Arimoto, N., Sadakane, K. et al. 2009a, A&A, 502, 569

Aoki, W., Barklem, P. S., Beers, T. C. et al. 2009b, ApJ, 698, 1803

Asplund, M., Grevesse, N., Sauval, A. J. & Scott, P., 2009, ARA&A, 47, 481

Bullock, J. S. & Johnston, K. V. 2005, ApJ, 635, 931

Beers, T. C., Chiba, M., Yoshii, Y. et al. 2000, AJ, 119, 2866

Beers, T. C., Carollo, D., Ivezić, Ẑ, et al. 2012, ApJ, 746, 34

Bell, E. F., Zucker, D. B., Belokurov, V. et al. 2008, ApJ, 680, 295

Belokurov, V., Zucker, D. B., Evans, N. W., et al. 2006, 642, L137

Bensby, T., Feltzing, S. & Lundström, I. 2003, A&A, 410, 527

Bensby, T., Zenn, A. R., Oey, M. S., & Feltzing, S. 2007, ApJ, 663L, 13

Bensby, T., Johnson, J. A., Cohen, J. et al. 2009, A&A, 499, 737

Bensby, T., Feltzing, S., Johnson, J. A. et al. 2010, A&A, 512, 41

Bensby, T., Adén, D., Meléndez, J. et al. 2011, A&A, 533, 134

Bergemann, M., 2011, MNRAS, 413, 2184

Bergemann, M., Lind, K., Collet, R., & Asplund, M. 2011, J. Phys. Conf. Ser., 328, 012002

Bonifacio, P., Spite, M., Cayrel, R. et al. 2009, A&A, 501, 519

Carney, B. W., Latham, D. W., Laird, J. B. & Aguilar, L. A. 1994, AJ, 107, 2240

Carollo, D., Beers, T. C., Lee, Y. S., et al. 2007, Nature, 450, 1020

Carollo, D., Beers, T. C., Chiba, M. 2010, ApJ, 712, 692

Casagrande, L., Ramírez, I., Meléndez, J., Bessell, M. & Asplund, M. 2010, A&A, 512, 54

Castelli, F. & Kurucz, R. L. 2003, in IAU Symp., Modelling of Stellar Atmosphere, ed. N. Piskunov (Cambridge Univ. Press), 210P, A20

Cayrel, R., Depagne, E., Spite, M. et al. 2004, A&A, 416, 1117

Chiba, M. & Beers, T. C. 2000, AJ, 119, 2843

Cooper, A. P., Cole, S., Frenk, C. S. et al. 2010, MNRAS, 406, 744

Cote, P., Marzke, R. O., West, M. J. & Minniti, D. 2000, ApJ, 533, 869

Cutri, R. M., Skrutskie, M. F., van Dyk, S. et al., 2003, yCat, 2246, 0

De Lucia, G. & Helmi, A. 2008, MNRAS, 391, 14

Dettbarn, C., Fuchs, B., Flynn, C. & Williams, M. A&A, 474, 857

Demarque, P., Woo, J.-H., Kim, Y.-C., & Yi, S. K. 2004, ApJS, 155, 667

Diemand, J., Kuhlen, M. & Madau, P., 2007, ApJ, 667, 859

Edvardsson, B., Andersen, J., Gustafsson, B., Lambert, D. L., Nissen, P. E., & Tomkin, J. 1993, A&A, 275, 101

Eggen, O. J., Lynden-Bell, D. & Sandage, A. R., ApJ, 136, 748

Feltzing, S., Eriksson, K., Kleyna, J. & Wilkinson, M. I. 2009, 508, L1

Font, A. S., Johnston, K. V., Bullock, J. S. & Robertson, B. E. 2006a, ApJ, 638, 585

Font, A. S., Johnston, K. V., Guhathakurta, P., Majewski, S. R. & Rich, R. M. 2006, AJ, 131, 1436

Font, A. S., Johnston, K. V., Bullock, J. S. & Robertson, B. E. 2006c, ApJ, 646, 886

Font, A. S., McCarthy, I. G., Crain, R. A. et al. 2011, MNRAS, 416, 2802

Freeman, K. C. & Bland-Hawthorn, J. 2002, ARA&A, 40, 487

Fuhr, J. R. & Wiese, W. L. 2006, JPCRD, 35, 1669

Fulbright, J.P. 2002, AJ, 123, 404

Fulbright, J. P., McWilliam, A. & Rich, R. M. 2007, ApJ, 661, 1152

Fuhrmann, K. 2011, MNRAS, 414, 2893

Garz, T. 1973, A&A, 26, 471

Gilmore, G., & Wyse, R. F. G. 1991, ApJ, 367, L55

Gratton, R. G., Carretta, E., Desidera, S., Lucatello, S., Mazzei, P. & Barbieri, M. 2003, A&A, 406, 131

Gustafsson, B., Edvardsson, B., Eriksson, K. et al. 2008,A&A, 489, 951

Hosford, A., Ryan, S. G., García Pérez, A. E., Norris, J. E., & Olive, K. A. 2009, A&A, 493, 601

Heiter, U. & Eriksson, K. 2006, A&A, 452, 1039

Helmi, A., White, S. D. M., de Zeeuw, T. & Zhao, H. Nature, 402, 53

Høg, E. et al. 2000, A&A, 355, L27

Hollek, J. K., Frebel, A., Roederer, I. U. et al. 2011, arXiv1108.4422

Ibata, R., Gilmore, G. & Irwin, M. 1994, Nature, 370, 194

Ishigaki, M., Chiba, M. & Aoki, W. 2010, PASJ, 62, 143

Ivans, I. I., Simmerer, J., Sneden, C. et al. 2006, ApJ, 645, 613

Johnston, K. V., Bullock, J. S., Sharma, S., et al. 2008, ApJ, 689, 936

Jurić, M., Ivezić, Ž., Brooks, A. et al. 2008, ApJ, 673, 864

Kepley, A. A. et al. 2007, AJ, 134, 1579

Kinman, T. D., Cacciari, C., Bragaglia, A., Smart, R., & Spagna, A. 2012, arXiv:1203.2146

Kirby, E. N., Guhathakurta, P., Simon, J. D. et al. 2010, ApJS, 191, 352

Kirby, E. N., Cohen, J. G., Smith, G. H. et al. 2011, ApJ, 727, 79

Klement, R., Rix, H.-W., Fuchs, B. et al. 2009, ApJ, 69 865

Kobayashi, C., Umeda, H., Nomoto, K., Tominaga, N., & Ohkubo, T. 2006, ApJ, 653, 1145

Kobayashi, C. & Nakazato, N. 2011, ApJ, 729, 16

Koch, A., McWilliam, A., Grebel, E. K. et al. 2008, ApJ, 688, L13

Lai, D. K., Bolte, M., Johnson, J. A. et al. 2008, ApJ, 681, 1524

Lai, D. K., Lee, Y. S., Bolte, M. et al. 2011, ApJ, 738, 51

Lanfranchi, G. A., & Matteucci, F. 2003, MNRAS, 345, 71

Lanfranchi, G. A., Matteucchi, F., & Cescutti, G. 2008, A&A, 481, 635

Lee, Y. S., Beers, T. C., Allende Prieto, C. et al. 2011, AJ, 141, 90

Lee, Y-W., Gim, H. B. & Casetti-Dinescu, D. I. 2007, ApJ, 661, L49

Lépine, S. et al. 2005, AJ, 129, 1483

Letarte, B., Hill, V., Tolstoy, E. et al. 2010, A&A, 523, 17

Martin, J. C. & Morrison, H. L. 1998, AJ, 116, 1724

Mashonkina, L., Gehren, T., Shi, J.-R., Korn, A. J. & Grupp, F. 2011, A&A, 528, 87

Matteucci, F. & Greggio, L. 1986, A&A, 154, 279

Monet, G. D et al. 2003, AJ, 125, 984

Mackey, A. D. & Gilmore, G. F. 2004, MNRAS, 355, 504

Majewski, S. R., Skrutskie, M. F., Weinberg, M. D. & Ostheimer, J. C. 2003, ApJ, 599, 1082

McWilliam, A. 1998, AJ, 1998, 115, 1640

Melendez, J., Asplund, M., Alves-Brito, A., et al. 2008, A&A, 484, 21

Melendez, J. & Barbuy, B. 2009, A&A, 497, 611

Morrison, H. L. et al. 2009, ApJ, 694, 130

Newberg, H. J., Yanny, B., Rockosi, C. 2002, ApJ, 569, 245

Nissen, P. E. & Schuster, W. J. 1997, A&A, 326, 751

Nissen, P. E., Hoeg, E., & Schuster, W. J. 1997, ESASP, 402, 225

Nissen, P. E., Akerman, C., Asplund, M., Fabbian, D., Kerber, F., Käufl, H. U., & Pettini, M. 2007, A&A, 469, 319

Nissen, P. E. & Schuster, W. J. 2010, A&A, 511, 10 (NS10)

Nissen, P. E. & Schuster, W. J. 2011, A&A, 530, 15

Noguchi, K., Aoki, W., Kawanomoto, S. et al. 2002, PASJ, 54, 855

Norris, J. E., Wyse, R. F. G., Gilmore, G. et al. 2010, ApJ, 723, 1632

Pickering, J. C., Thorne, A. P. & Perez, R. 2001, ApJS, 132, 403

Purcell, C. W., Bullock, J. S. & Kazantzidis, S. 2010, MNRAS, 404, 1711

Ramírez, I. & Meléndez, J. 2005, ApJ, 626, 465

Reddy, B. E., Lambert, D. L. & Allende Prieto, C. 2006, MNRAS, 367, 1329

Reddy, B. E. & Lambert, D. L. 2008, MNRAS, 391, 95

Robertson, B., Bullock, J. S., Font, A. S., Johnston, K. V. & Hernquist, L., ApJ, 2005, 632, 872

Roederer, I. U. 2008, AJ, 137, 272

Ruchti, G. R., Fulbright, J. P., Wyse, R. F. G. et al. 2011, ApJ, 737, 9

Ryan, S. G. & Norris, J. E. 1991, AJ, 101, 1835

Schlaufman, K. C. et al. 2009, ApJ, 703, 2177

Schönrich, R., Asplund, M., & Casagrande, L. 2011, MNRAS, 415, 3807

Searle, L. & Zinn, R. 1978, ApJ, 225, 357

Shetrone, M. D., Cote, P. & Sargent, W. L. W. 2001, ApJ, 548, 529

Shetrone, M. D., Venn, K. A., Tolstoy, E. et al. 2003, ApJ, 125, 684

Schuster, W. J., Moreno, E., Nissen, P. E., & Pichardo, B. 2011, arXiv:1111.4026

Stephens, A. & Boesgaard, A. M. 2002, AJ, 123, 1647

Starkenburg, E. et al. 2009, ApJ, 698, 567

Tinsley, B. M. 1979, ApJ, 229, 1046

Tolstoy, E., Venn, K. A., Shetrone, M., Hill, V., Kaufer, A., & Szeifert, T. 2003, AJ, 125, 707

Tolstoy, E., Hill, V. & Tosi, M. 2009, ARA&A, 47, 371

Tsujimoto, T., Nomoto, K., Yoshii, Y., Hashimoto, M., Yanagida, S., & Thielemann, F. K. 1995, MNRAS, 277, 945

van Leeuwen, F. 2007, A&A, 474, 653

Venn, K. A., Irwin, M., Shetrone, M. D. et al. 2004, AJ, 128, 1177

Xue, X.-X., Rix, H.-W., Yanny, B. et al. 2011, ApJ, 738, 79

Zacharias, N. et al. 2004, AJ, 127, 3043

Zhang, L., Ishigaki, M., Aoki, W., Zhao, G. & Chiba, M. 2009, ApJ, 706, 1095

Zolotov, A., Willman, B., Brooks, A. et al. 2010, ApJ, 721, 738

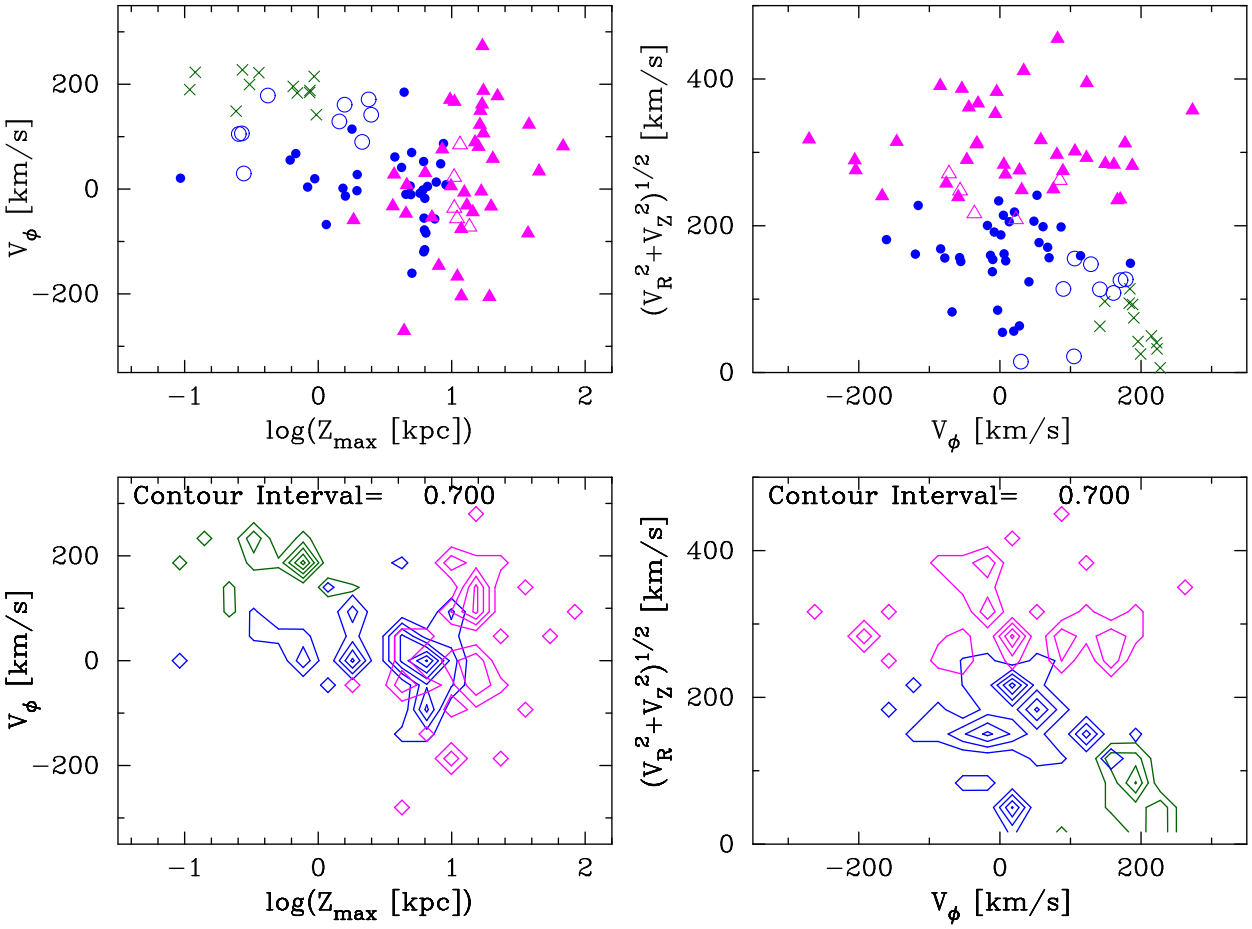

Fig. 1.— Kinematics of the sample stars. The top panels show the $\log(Z_{\rm max}) - V_\phi$ (left) and $V_\phi - (V_R^2 + V_Z^2)^{1/2}$ (right) diagram. Crosses, filled circles and filled triangles indicate the sample stars with $P_{\rm TD} > 0.9$ (the thick disk stars), $P_{\rm IH} > 0.9$ (the inner halo stars) and $P_{\rm OH} > 0.9$ (the outer halo stars), respectively. Open circles show the stars whose kinematics are intermediate between the thick disk and the inner halo ($P_{\rm TD}, P_{\rm IH} \leq 0.9$ and $P_{\rm TD}$, $P_{\rm IH} \geq P_{\rm OH}$), while open triangles indicate stars whose kinematics are intermediate between the inner and the outer halo ($P_{\rm IH}$, $P_{\rm OH} \leq 0.9$ and $P_{\rm IH}$, $P_{\rm OH} \geq P_{\rm TD}$). The lower panels show the distributions of the $P_{\rm TD}$ (green), $P_{\rm IH}$(blue) and $P_{\rm OH}$ (magenta), in the same diagrams as the top panels. Each contour shows sum of the membership probability within a given bin of the kinematic parameter.

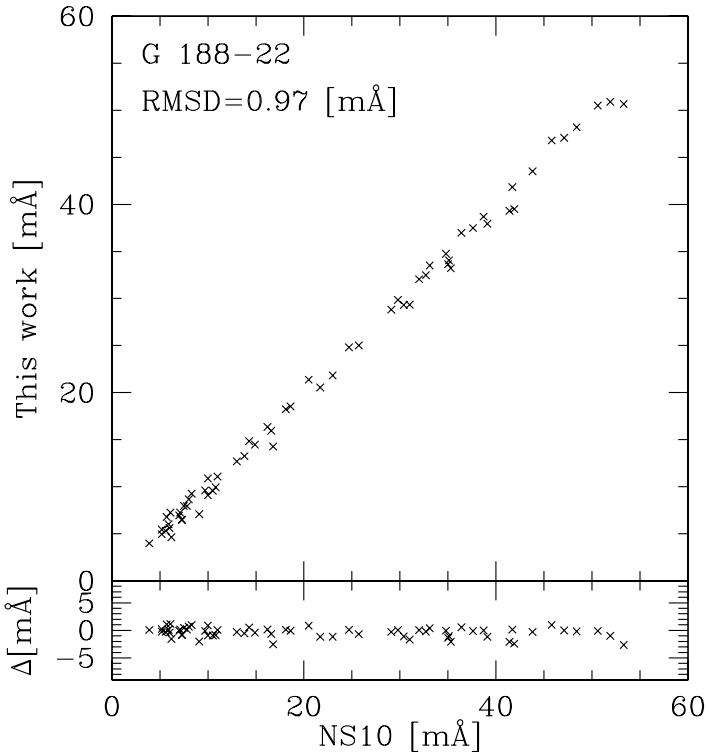

Fig. 2.— Comparison of the measured EWs in this work and those measured in Nissen & Schuster (2010)

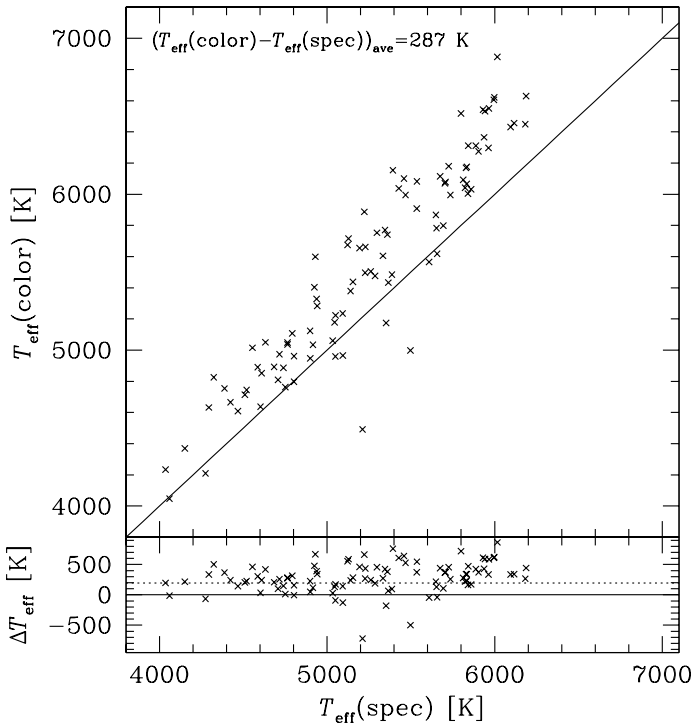

Fig. 3.— Comparison of the color and spectroscopic $T_{\rm eff}$; the top panel shows a plot of $T_{\rm eff}$ estimated from V-K with that estimated from the abundance-χ relation of Fe I lines. The bottom panel plots differences of the two $T_{\rm eff}$ estimates. The mean of the differences is shown as a dotted line.

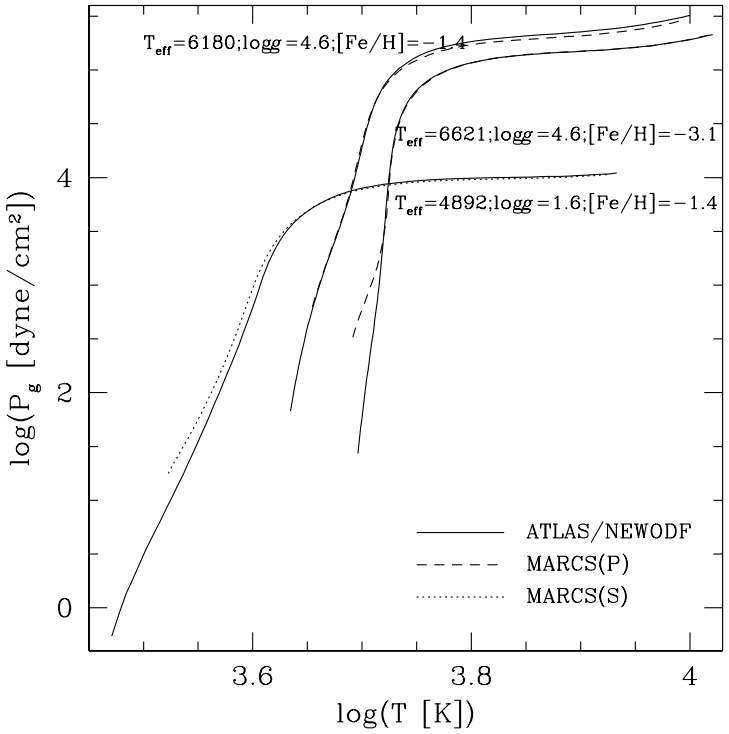

Fig. 4.— Comparison of the Kurucz NEWODF model atmosphere, adopted in this work, with MARCS model atmosphere for three stars in our sample, G 24–3 ($T_{\rm eff}$ = 6180 K, $\log g$ = 4.6 dex and [Fe/H]= −1.4), HD 215601 ($T_{\rm eff}$ = 4892 K, $\log g$ = 1.6 dex and [Fe/H]= −1.4) and G 64–37 ($T_{\rm eff}$ = 6621 K, $\log g$ = 4.6 dex and [Fe/H]= −3.1). Solid, dashed and dotted lines show $T - P_g$ relations for the model atmospheres of ATLAS/NEWODF, MARCS/Plain-Parallel and MARCS/Spherical, respectively. The differences in derived abundance ratios are given in the last column of Table 7.

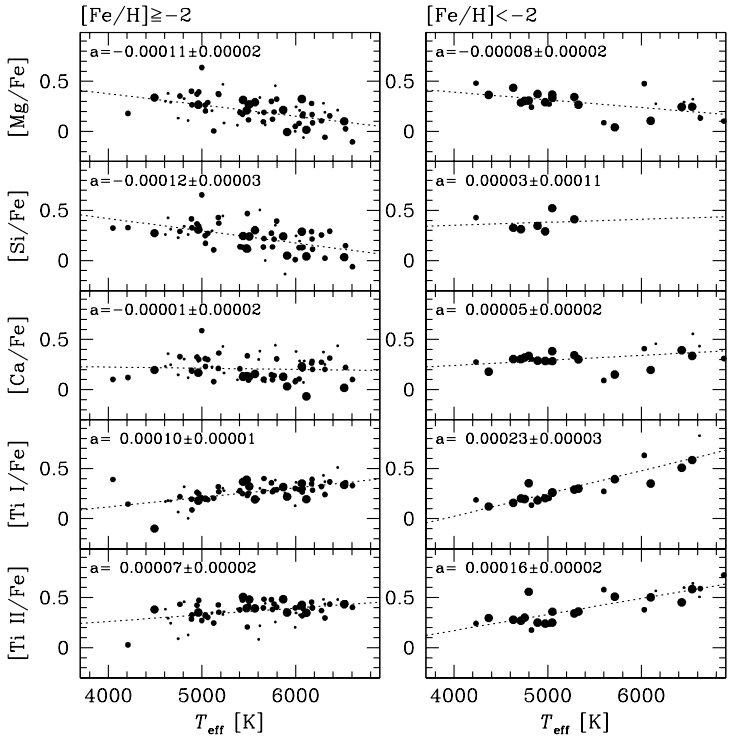

Fig. 5.— [X/Fe] ratios plotted against $T_{\rm eff}$ values for the sample stars with the metallicity [Fe/H]≥ -2 (left) and [Fe/H]< -2 (right). Size of the symbols corresponds to metallicity; for the left (right) panel, small:$-2.0 \leq$[Fe/H]< -1.5 ([Fe/H]< -3.0), medium:$-1.5 \leq$[Fe/H]< -1.0 ($-3.0 \leq$[Fe/H]< -2.5), and large:$-1.0 \geq$[Fe/H] ($-2.5 \leq$[Fe/H]< -2.0). Dotted line in each panel shows the result of a least square fit to a straight line [X/Fe]$= b + aT_{\rm eff}$. The slope a of the fit is indicated in the each panel.

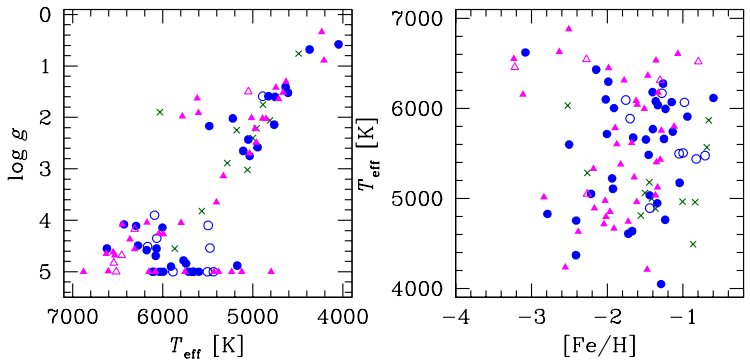

Fig. 6.— The $\log g$ vs. $T_{\rm eff}$ (left) and $T_{\rm eff}$ vs. [Fe/H] (right) diagrams for the sample stars. Symbols are the same as in the top panels of Figure 1.

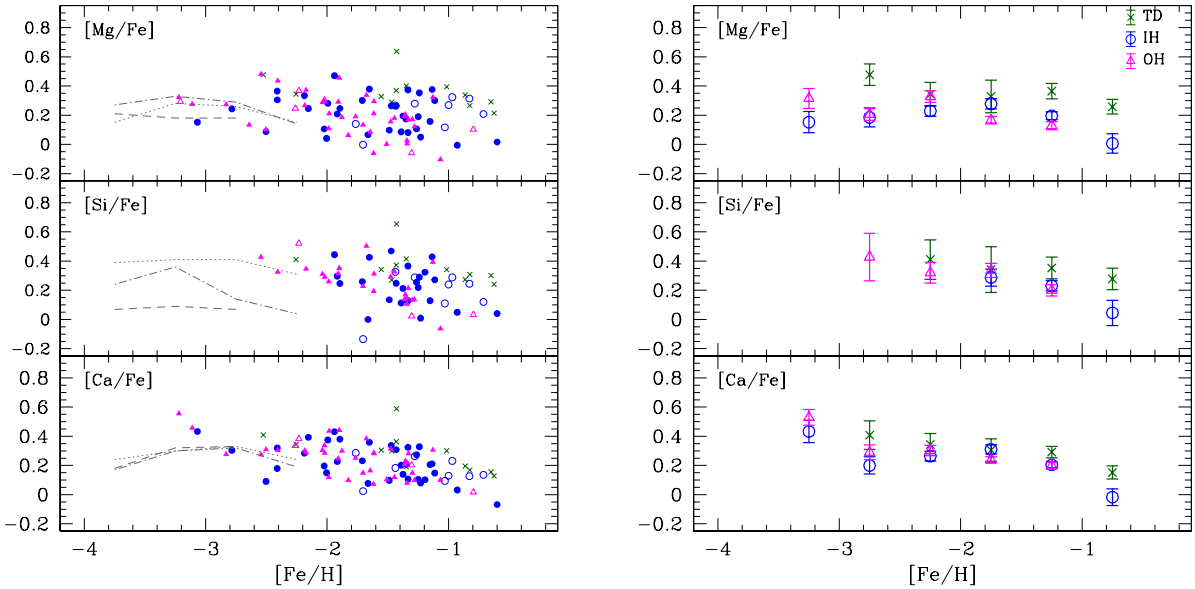

Fig. 7.— *left*: α-elements (Mg, Si, Ca) to iron abundance ratios as a function of [Fe/H]. Symbols are the same as in the top panels of Figure 1. Mean values of the abundance ratios within a given metallicity interval obtained by Cayrel et al. (2004), Lai et al. (2008) and Bonifacio et al. (2009) are connected with dotted, dash-dotted and dashed lines, respectively. *Right*: Weighted mean of the [Mg/Fe], [Si/Fe] and [Ca/Fe] in each [Fe/H] interval for the sample stars with $P_{\rm TD} > 0.9$ (crosses), $P_{\rm IH}$ (circles) and $P_{\rm OH} > 0.9$ (triangles).

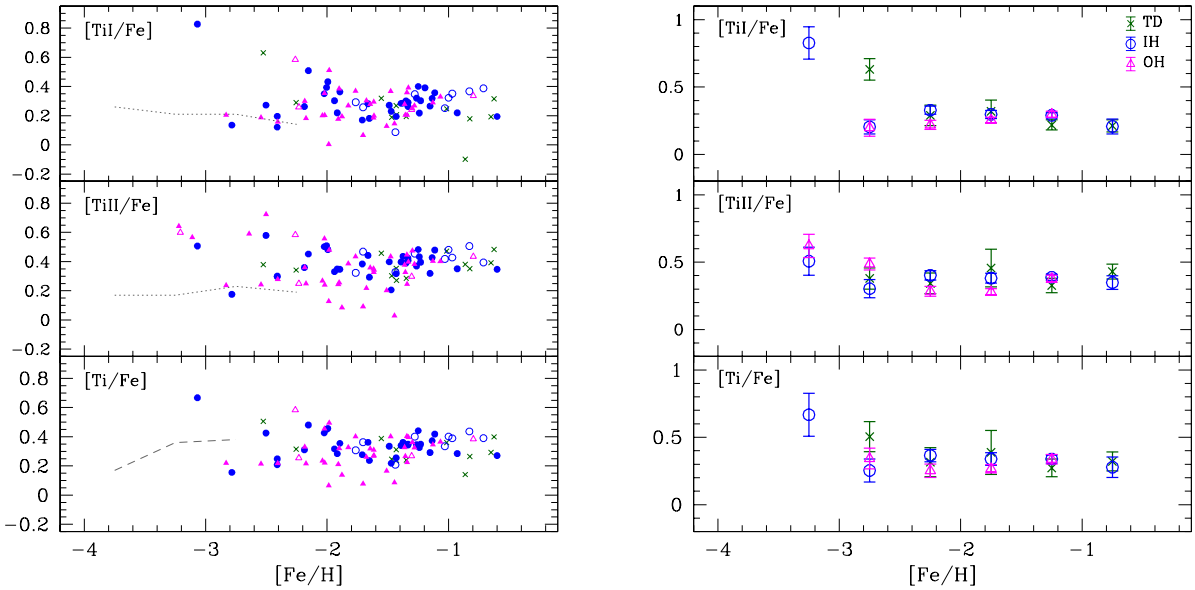

Fig. 8.— Same as Figure 7 but for [Ti I/Fe], [Ti II/Fe] and [Ti/Fe] =([Ti I/Fe]+[Ti II/Fe]) / 2.

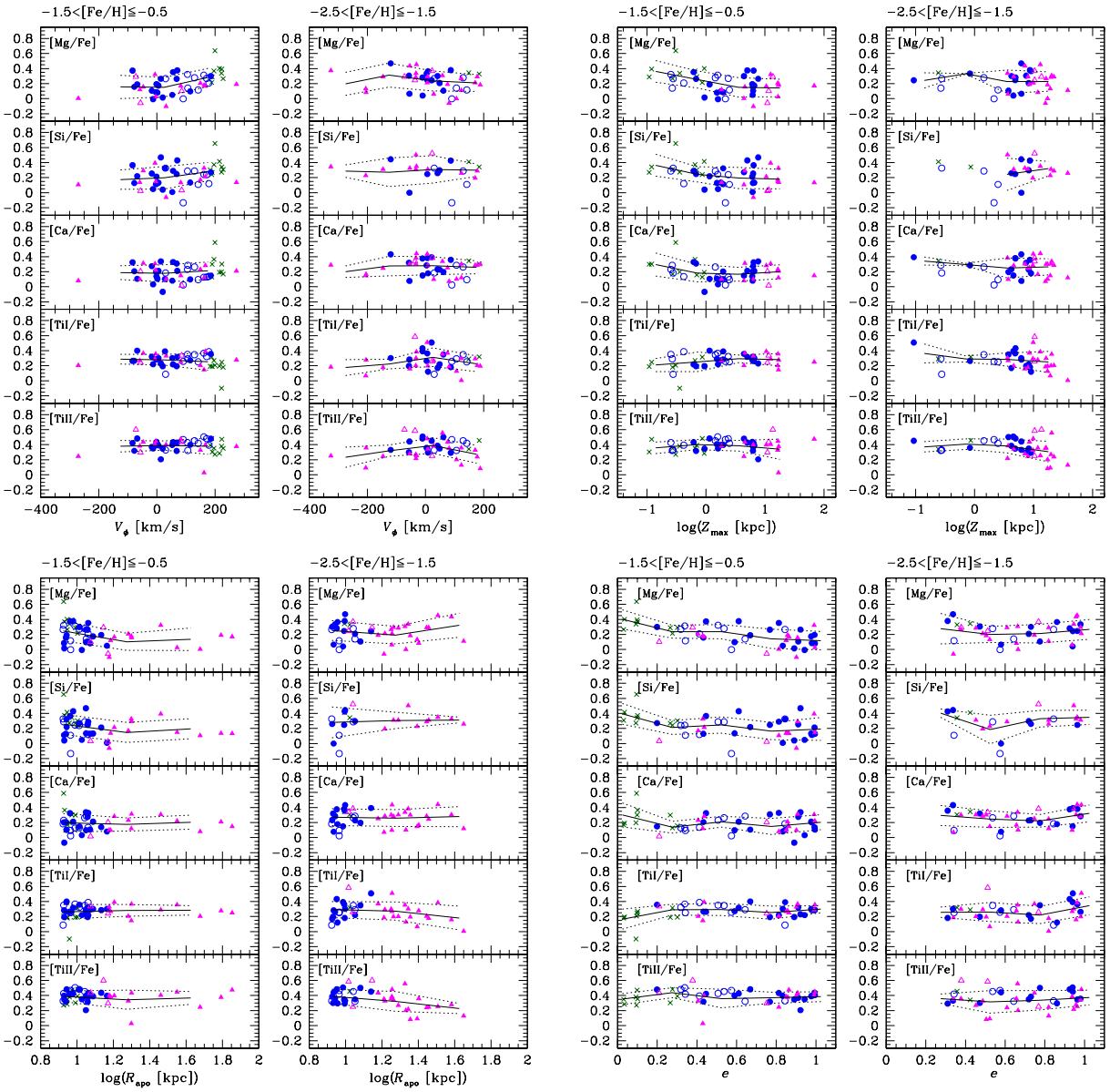

Fig. 9.— The [α/Fe] ratios plotted against V_ϕ (top left), $\log Z_{\rm max}$ (top right), $\log R_{\rm apo}$ (bottom left) and e (bottom right). Symbols are the same as in the top panels of Fig.1. Solid and dashed lines connect means and means $\pm$ standard deviations, respectively, within a given interval of each orbital parameter.

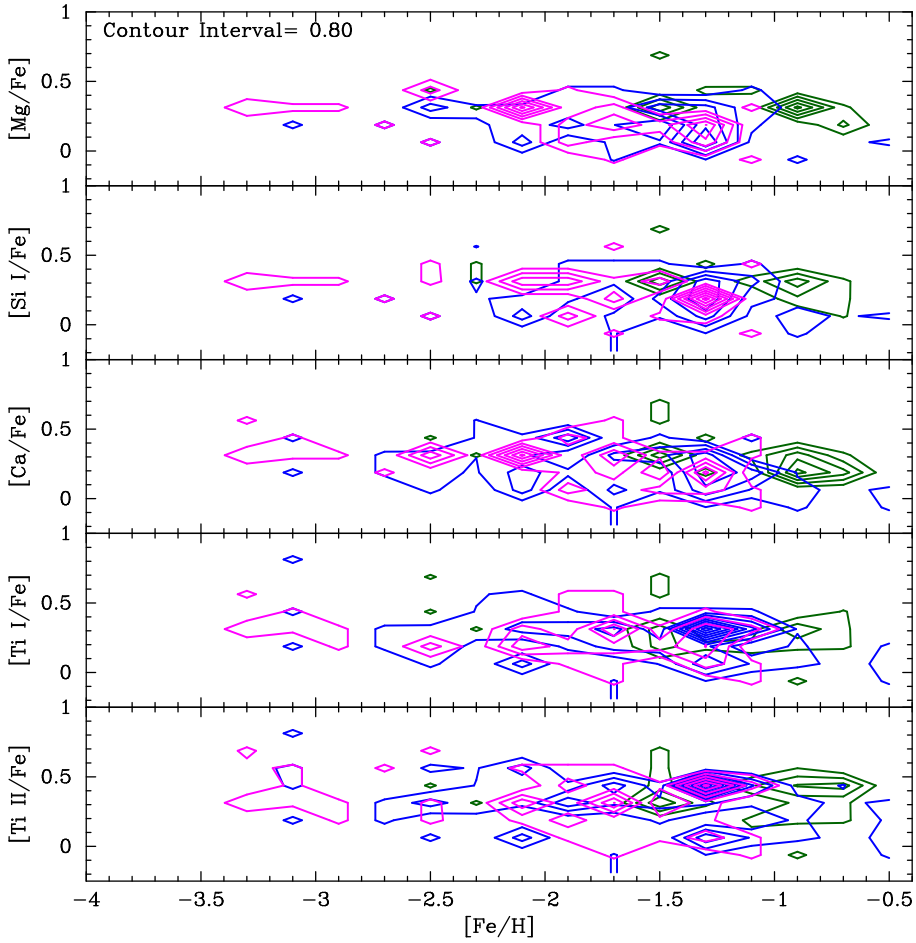

Fig. 10.— Distribution for $P_{\rm TD}$ (green), $P_{\rm IH}$ (blue) and $P_{\rm OH}$ (magenta) in [X/Fe]-[Fe/H] planes. Each contour shows sum of the membership probability within a given [X/Fe] and [Fe/H] bin.

Table 1. Mean Velocities and Dispersions for the Thick disk, Inner, and Outer halo components adopted from Carollo et al. (2010)

Component	$< V_R >$[a] (km s^{-1})	$< V_\phi >$ (km s^{-1})	$< V_Z >$ (km s^{-1})	σ_R[b] (km s^{-1})	σ_ϕ (km s^{-1})	σ_Z (km s^{-1})	f_i ($Z_{\rm max}$ kpc)[c]				
							< 5	$5-10$	$10-15$	$15-20$	> 20
Thick disk	3	182	0	53	51	35	0.55	0.00	0.00	0.00	0.00
Inner halo	3	7	3	150	95	85	0.45	1.00	0.80	0.55	0.08
Outer halo	-9	-80	2	159	165	116	0.00	0.00	0.20	0.45	0.92

Note. —

[a]Mean velocities in a cylindrical coordinate.

[b]Velocity dispersions in a cylindrical coordinate.

[c]Fractional contribution of stars at a given $Z_{\rm max}$ range.

Table 2. Kinematics of the sample

Object name	[Fe/H][a] (dex)	$V_{\rm rad}$[b] (km s^{-1})	V_R (km s^{-1})	V_ϕ (km s^{-1})	V_Z (km s^{-1})	$P_{\rm TD}$[c]	$P_{\rm IH}$	$P_{\rm OH}$
BD+01°3070	−1.37	−328.4 ± 0.3	338.9 ± 24.1	273.0 ± 11.1	−113.2 ± 22.8	0.00	0.00	1.00
BD–03°5215	−1.48	−296.5 ± 0.3	147.5 ± 1.8	13.2 ± 7.4	143.1 ± 7.8	0.00	1.00	0.00
BD+04°2466	−1.95	33.4 ± 0.5	−56.6 ± 8.7	−119.7 ± 68.3	−151.1 ± 37.6	0.00	1.00	0.00
BD+04°2621	−2.39	−40.0 ± 0.3	−1.7 ± 10.3	−57.0 ± 61.4	−156.5 ± 25.6	0.00	1.00	0.00
BD–08°3901	−1.56	−108.9 ± 0.3	109.6 ± 8.5	184.3 ± 13.1	−31.3 ± 7.1	0.92	0.08	0.00

Note. — Table 2 is published in its entirety in the electronic edition of the Astrophysical Journal. A portion is shown here for guidance regarding its form and context.

[a][Fe/H] estimated from the high-resolution spectra obtained with Subaru/HDS.

[b]Radial velocities measured from the high-resolution spectra obtained with Subaru/HDS.

[c]See Section 2.2.2.

Table 3. Summary of the new observation

Object name	RA	DEC	V (mag)	Date	Exp.time (s)	N[a]	S/N[b]
G176–53	11:46:34.100	+50:52:36.52	9.92	2010-05-26	900	1	269
HD 103295	11:53:37.900	−28:38:01.05	9.58	2010-05-26	900	1	291
HD 233891	11:59:58.915	+51:46:05.04	8.80	2010-05-26	400	1	280
HD 105004	12:05:25.548	−26:35:36.09	10.31	2010-05-26	600	2	180
G59–1	12:08:54.954	+21:47:11.97	9.52	2010-05-26	900	1	302
HD 105546	12:09:02.284	+59:00:50.97	8.61	2010-05-26	400	1	302
HD 106373	12:14:14.150	−28:14:56.36	8.91	2010-05-26	600	1	349
HD 108317	12:26:37.563	+05:18:08.16	8.03	2010-05-26	200	2	299
HD 108976	12:31:03.580	+27:43:40.09	8.56	2010-05-26	400	1	353
HD 109995	12:38:47.757	+39:18:18.84	7.60	2010-05-26	200	1	383
G60–26	12:40:00.196	+12:38:26.17	9.82	2010-05-26	900	1	284
HD 112126	12:53:49.591	+32:30:17.23	8.74	2010-05-26	400	1	279
G14–33	13:08:48.852	−03:58:09.48	11.18	2010-05-26	1200	2	177
HD 116064	13:21:44.254	−39:18:29.20	8.81	2010-05-26	600	1	332
BD+09°2776	13:33:32.853	+08:35:09.18	7.96	2010-05-26	300	1	360
G63–46	13:40:00.438	+12:35:13.22	9.39	2010-05-26	600	1	280
HD 122196	14:01:02.773	−38:02:52.04	8.72	2010-05-26	415	1	283
HD 122956	14:05:13.431	−14:51:09.25	7.22	2010-05-26	100	1	288
G66–51	15:00:50.751	+02:07:35.50	10.63	2010-05-26	600	2	161
BD-08°3901	15:04:52.065	−08:48:56.60	9.47	2010-05-26	600	1	261
G153–21	16:03:00.868	−06:27:06.83	10.19	2010-05-26	600	2	196
HD 171496	18:36:08.100	−24:25:55.66	8.49	2010-05-26	400	1	299
LP 751-19	18:51:09.320	−11:48:06.99	10.42	2010-05-26	600	2	156
LTT 15637	19:15:07.514	+10:34:46.43	9.42	2010-05-26	600	1	272
HD 184266	19:34:15.916	−16:18:44.80	7.59	2010-05-26	200	1	331
G142–44	19:38:53.270	+16:25:52.01	11.15	2010-06-18	1000	2	155
G23–14	19:51:49.475	+05:37:01.20	10.71	2010-06-18	800	2	173
HD 188510	19:55:09.157	+10:44:44.85	8.83	2010-05-26	400	1	250
G24–3	20:05:43.948	+04:03:05.98	10.46	2010-05-26	600	2	153
HD 193901	20:23:36.569	−21:22:08.94	8.66	2010-05-26	400	1	254
HD 196892	20:40:49.665	−18:47:21.00	8.25	2010-05-26	400	1	347
G210–33	20:45:21.964	+40:23:19.68	11.20	2010-06-18	900	2	153
BD-14°5850	20:47:35.059	−14:25:35.90	10.96	2010-06-18	700	2	148
G212–7	20:55:15.410	+42:17:54.06	10.27	2010-05-26	600	2	174
HD 199854	21:00:13.794	−15:06:35.32	8.95	2010-05-26	600	1	309
G187–40	21:21:56.700	+27:27:12.45	10.51	2010-06-18	600	2	164
BD+46°3330	21:28:47.483	+47:06:53.65	9.30	2010-05-26	600	1	325
G231–52	21:39:13.871	+60:16:56.82	10.34	2010-06-18	500	2	149
G188–22	21:43:56.002	+27:23:33.22	10.05	2010-05-26	600	2	193
BD+47°3617	21:57:01.410	+48:22:46.66	10.30	2010-06-18	500	2	214
BD+46°3563	22:04:13.870	+47:24:13.38	10.10	2010-06-18	900	1	292
HD 210295	22:09:41.566	−13:36:03.37	9.57	2010-05-26	900	1	260
HD 213487	22:32:03.550	−21:35:40.04	9.87	2010-05-26	900	1	235
HD 213467	22:32:08.605	−31:10:10.22	8.52	2010-05-26	400	1	286
HD 215601	22:46:48.598	−31:52:04.73	8.46	2010-05-26	400	1	311

[a]Number of exposures.

[b]Signal-nose-ratio per resolution element.

Table 4. Equivalent widths

Object name	Z/Ion	Element	λ (Å)	$\log gf$ (dex)	χ (eV)	EW (Å)	Flag[a]	Refs.[b]
BD+01°3070	26 1	FeI	4114.44	−1.30	2.83	55.69	1	O91
BD+01°3070	26 1	FeI	4132.90	−1.01	2.84	66.03	1	O91
BD+01°3070	26 1	FeI	4147.67	−2.10	1.48	79.11	1	B80
BD+01°3070	26 1	FeI	4184.89	−0.87	2.83	70.24	1	O91
BD+01°3070	26 1	FeI	4222.21	−0.97	2.45	84.88	0	B82a

Note. — Table 4 is published in its entirety in the electronic edition of the Astrophysical Journal. A portion is shown here for guidance regarding its form and context.

[a]1: Used in the abundance analysis, 0: Not used in the abundance analysis.

[b]Reference of adopted $\log gf$. A complete list of references are given in the electronic version of this table.

Table 5. Atmospheric parameters and abundances

Object name	$T_{\rm eff}$ (K)	$\log g$ (dex)	ξ (km s^{-1})	[Fe I/H] (dex)	[Fe II/H] (dex)	[Mg/Fe] (dex)	[Si/Fe] (dex)	[Ca/Fe] (dex)	[Ti I/Fe] (dex)	[Ti II/Fe] (dex)
BD+01°3070	5404	3.65	1.18	-1.38 ± 0.14	-1.36 ± 0.13	0.19 ± 0.11	0.14 ± 0.15	0.21 ± 0.08	0.28 ± 0.08	0.38 ± 0.08
BD+04°2466	5223	2.02	1.72	-1.95 ± 0.14	-1.94 ± 0.12	0.47 ± 0.10	0.44 ± 0.12	0.43 ± 0.08	0.30 ± 0.10	0.33 ± 0.11
BD+04°2621	4754	1.63	1.72	-2.37 ± 0.16	-2.41 ± 0.12	0.30 ± 0.09	-9.99 ± 0.00	0.32 ± 0.09	0.20 ± 0.08	0.30 ± 0.09
BD+09°2870	4632	1.30	1.63	-2.37 ± 0.17	-2.41 ± 0.12	0.43 ± 0.09	0.33 ± 0.14	0.30 ± 0.09	0.16 ± 0.08	0.28 ± 0.09
BD+10°2495	4973	2.25	1.64	-2.02 ± 0.15	-2.02 ± 0.12	0.29 ± 0.09	0.29 ± 0.14	0.29 ± 0.08	0.20 ± 0.08	0.24 ± 0.07

Note. — Table 5 is published in its entirety in the electronic edition of the Astrophysical Journal. A portion is shown here for guidance regarding its form and context.

Table 6. Comparison with NS10

Starname	NS10/TW	$T_{\rm eff}$ (K)	$\log g$ (dex)	ξ (km s^{-1})	[Fe/H] (dex)	[Mg/Fe] (dex)	[Si/Fe] (dex)	[Ca/Fe] (dex)	[Ti/Fe] (dex)	$U^{\rm a}$ (km s^{-1})	$V^{\rm a}$ (km s^{-1})	$W^{\rm a}$ (km s^{-1})	Classification
G 112–43	NS10	6074	4.03	1.30	−1.25	0.21	0.15	0.29	0.29	−145	−119	−293	low-alpha
	TW	6176	4.05	1.36	−1.33	0.17	0.21	0.28	0.39	−126	−52	−197	OH
G 53–41	NS10	5859	4.27	1.30	−1.20	0.24	0.24	0.31	0.14	31	−299	−150	low-alpha
	TW	6070	4.56	0.77	−1.15	0.16	0.13	0.21	0.27	27	−298	−153	IH
G 125–13	NS10	5848	4.28	1.50	−1.43	0.30	0.28	0.30	0.20	−215	−228	−157	(high-alpha)
	TW	6079	4.75	0.79	−1.35	0.17	0.13	0.21	0.30	−170	−217	−130	IH
HD111980	NS10	5778	3.96	1.50	−1.08	0.36	0.40	0.34	0.25	−239	−174	−57	high-alpha
	TW	5798	4.04	1.21	−1.13	0.32	0.39	0.31	0.29	−327	−224	−131	OH
G 20–15	NS10	6027	4.32	1.60	−1.49	0.22	0.23	0.29	0.24	−161	−60	−210	(low-alpha)
	TW	6042	4.26	1.22	−1.62	0.21	0.19	0.28	0.29	−150	−50	−183	OH
HD105004	NS10	5754	4.30	1.20	−0.82	0.17	0.14	0.17	0.07	44	−239	−92	low-alpha
	TW	6115	5.00	0.40	−0.60	0.02	0.04	−0.07	0.19	21	−200	−52	IH
G 176–53	NS10	5523	4.48	1.00	−1.34	0.15	0.15	0.25	0.15	230	−271	61	low-alpha
	TW	5753	5.00	0.17	−1.28	0.12	0.14	0.10	0.27	232	−279	60	OH
HD193901	NS10	5650	4.36	1.20	−1.09	0.13	0.18	0.22	0.10	148	−233	−66	low-alpha
	TW	5908	4.94	0.29	−0.93	−0.01	0.05	0.03	0.22	146	−233	−65	IH
G 188–22	NS10	5974	4.18	1.50	−1.32	0.39	0.37	0.37	0.28	−193	−99	71	high-alpha
	TW	6170	4.52	1.13	−1.28	0.28	0.29	0.26	0.35	−135	−93	62	IH/TD

[a]Adopted solar motions are $(U_\odot, V_\odot, W_\odot) = (-7.5, 13.5, 6.8)$ km s^{-1} in NS10 and $(-9, 12, 7)$ km s^{-1} in TW.

Table 7. Error estimates

Object name	$T_{\rm eff}$ (K)	$\log g$ (dex)	ξ (km s^{-1})	Element	Abundance (dex)	$\sigma_{T_{\rm eff}} \pm 100$ (dex)	$\sigma_{\log g} \pm 0.3$ (dex)	$\sigma_{\xi} \pm 0.3$ (dex)	MARCS (dex)
G24–3	6180	4.6	0.3	[Fe I/H]	−1.40	0.08	−0.06	−0.03	−0.03
						−0.09	0.06	···	
				[Fe II/H]	−1.39	0.02	0.08	−0.03	−0.04
						−0.02	−0.08	···	
				[Mg/Fe]	0.09	−0.03	0.01	0.02	0.06
						0.03	−0.00	···	
				[Si/Fe]	0.11	−0.06	0.08	0.03	0.01
						0.06	−0.07	···	
				[Ca/Fe]	0.20	−0.03	0.01	0.02	0.00
						0.03	−0.01	···	
				[Ti I/Fe]	0.28	0.00	0.05	0.01	0.01
						−0.00	−0.05	···	
				[Ti II/Fe]	0.40	0.03	−0.01	0.00	−0.03
						−0.03	0.01	···	
HD215601	4892	1.6	1.7	[Fe I/H]	−1.40	0.14	−0.02	−0.10	−0.16
						−0.14	0.03	0.13	
				[Fe II/H]	−1.44	−0.03	0.12	−0.07	−0.06
						0.03	−0.12	0.09	
				[Mg/Fe]	0.27	−0.07	0.00	0.07	0.06
						0.06	−0.00	−0.08	
				[Si/Fe]	0.33	−0.10	0.03	0.09	0.10
						0.10	−0.03	−0.12	
				[Ca/Fe]	0.18	−0.04	−0.01	0.02	0.05
						0.04	0.00	−0.04	
				[Ti I/Fe]	0.09	0.01	0.00	0.05	0.07
						−0.01	0.00	−0.06	
				[Ti II/Fe]	0.33	0.04	−0.01	−0.10	−0.07
						−0.04	0.01	0.12	
G64–37	6621	4.6	2.5	[Fe I/H]	−3.07	0.07	0.00	−0.01	0.01
						−0.07	0.00	0.01	
				[Fe II/H]	−3.07	0.01	0.10	−0.00	0.00
						−0.01	−0.10	0.00	
				[Mg/Fe]	0.15	−0.01	−0.02	−0.02	0.00
						0.01	0.01	0.03	
				[Ca/Fe]	0.43	−0.02	−0.00	0.00	−0.01
						0.02	0.00	−0.00	
				[Ti I/Fe]	0.83	0.01	−0.00	0.00	−0.00
						−0.01	0.00	−0.00	
				[Ti II/Fe]	0.51	0.02	−0.00	−0.00	0.01
						−0.03	0.00	0.00	
BD–18°271	4234	0.4	2.5	[Fe I/H]	−2.58	0.16	−0.05	−0.04	···
						−0.17	0.06	0.05	
				[Fe II/H]	−2.54	−0.03	0.11	−0.01	···
						0.04	−0.10	0.01	
				[Mg/Fe]	0.48	−0.07	0.01	0.03	···

Table 7—Continued

Object name	$T_{\rm eff}$ (K)	$\log g$ (dex)	ξ (km s^{-1})	Element	Abundance (dex)	$\sigma_{T_{\rm eff}} \pm 100$ (dex)	$\sigma_{\log g} \pm 0.3$ (dex)	$\sigma_{\xi} \pm 0.3$ (dex)	MARCS (dex)
						0.07	−0.01	−0.04	
				[Si/Fe]	0.43	−0.12	0.05	0.04	···
						0.14	−0.05	−0.05	
				[Ca/Fe]	0.28	−0.06	−0.00	0.01	···
						0.05	−0.00	−0.02	
				[Ti I/Fe]	0.19	0.06	0.00	0.01	···
						−0.06	−0.00	−0.02	
				[Ti II/Fe]	0.24	0.03	−0.02	−0.04	···
						−0.03	0.02	0.05	

Table 8. Means and standard deviations in the abundance ratios

[X/Fe]	TD/IH/OH	[Fe/H]> -1.5			$-2.5 <$[Fe/H]≤ -1.5			[Fe/H]≤ -2.5		
		μ[a]	σ[b]	N[c]	μ	σ	N	μ	σ	N
Mg	TD	0.32	0.07	8	0.34	0.01	2	0.48	0.00	1
	IH	0.18	0.12	17	0.26	0.13	13	0.16	0.08	3
	OH	0.13	0.12	11	0.22	0.14	20	0.27	0.14	6
Si	TD	0.32	0.06	8	0.38	0.05	2		···	
	IH	0.21	0.13	18	0.28	0.16	6		···	
	OH	0.18	0.12	11	0.31	0.08	11	0.43	0.00	1
Ca	TD	0.23	0.08	8	0.33	0.03	2	0.41	0.00	1
	IH	0.17	0.11	18	0.28	0.11	13	0.28	0.17	3
	OH	0.19	0.09	11	0.26	0.11	20	0.38	0.13	5
Ti I	TD	0.19	0.12	9	0.30	0.02	2	0.63	0.00	1
	IH	0.28	0.06	18	0.29	0.11	13	0.41	0.37	3
	OH	0.28	0.08	11	0.24	0.12	20	0.20	0.01	2
Ti II	TD	0.37	0.08	9	0.40	0.08	2	0.38	0.00	1
	IH	0.39	0.07	17	0.39	0.08	13	0.42	0.21	3
	OH	0.36	0.12	11	0.29	0.12	20	0.50	0.21	6

[a]Means of the abundance ratios within a given [Fe/H] interval.

[b]Standard deviations of the means.

[c]The number of stars used to calculate the μ and σ.